

# Neuronal Attention Circuit (NAC) for Representation Learning

Waleed Razzaq<sup>1</sup> Izis Kanjaraway<sup>1</sup> Yun-Bo Zhao<sup>1,2</sup>

## Abstract

Attention improves representation learning over RNNs, but its discrete nature limits continuous-time (CT) modeling. We introduce Neuronal Attention Circuit (NAC), a novel, biologically inspired CT-Attention mechanism that reformulates attention logit computation as the solution to a linear first-order ODE with nonlinear inter-linked gates derived from repurposing *C.elegans* Neuronal Circuit Policies (NCPs) wiring. NAC replaces dense projections with sparse sensory gates for key-query projections and a sparse backbone network with two heads for computing *content-target* and *learnable time-constant* gates, enabling efficient adaptive dynamics. To improve efficiency and memory consumption, we implemented an adaptable subquadratic sparse Top- $K$  pairwise concatenation mechanism that selectively curates key-query interactions. We provide rigorous theoretical guarantees, including state stability and bounded approximation errors. Empirically, we implemented NAC in diverse domains, including irregular time-series classification, lane-keeping for autonomous vehicles, and industrial prognostics. We observed that NAC matches or outperforms competing baselines in accuracy and occupies an intermediate position in runtime and memory consumption compared with several CT state-of-the-art baselines, while being interpretable at the neuron cell level.

## 1. Introduction

Learning representations of sequential data in temporal or spatiotemporal domains is essential for capturing patterns and enabling accurate forecasting. Discrete-time Recurrent neural networks (DT-RNNs), such as RNN (Rumelhart et al., 1985; Jordan, 1997), Long-short term memory

<sup>1</sup>Department of Automation, University of Science & Technology of China, Hefei, China <sup>2</sup>Institute of Artificial Intelligence, Hefei Comprehensive National Science Center. Correspondence to: Yun-Bo Zhao <ybzha@ustc.edu.cn>, Waleed Razzaq <waleedrazzaq@mail.ustc.edu.cn>.

(LSTM) (Hochreiter & Schmidhuber, 1997), and Gated Recurrent Unit (GRU) (Cho et al., 2014) model sequential dependencies by iteratively updating hidden states to represent or predict future elements in a sequence. While effective for regularly sampled sequences, DT-RNNs face challenges with irregularly sampled data because they assume uniform time intervals. In addition, vanishing gradients can make it difficult to capture long-term dependencies (Hochreiter, 1998).

Continuous-time RNNs (CT-RNNs) (Rubanova et al., 2019) model hidden states as ordinary differential equations (ODEs), allowing them to process inputs that arrive at arbitrary or irregular time intervals. Mixed-memory RNNs (mmRNNs) (Lechner & Hasani, 2022) build on this idea by separating memory compartments from time-continuous states, helping maintain stable error propagation while capturing continuous-time dynamics. Liquid neural networks (LNNs) (Hasani et al., 2021; 2022) take a biologically inspired approach by assigning variable time-constants to hidden states, improving adaptability and robustness, although vanishing gradients can still pose challenges during training. The attention mechanisms (Vaswani et al., 2017) mitigate this limitation by treating all time steps equally and allowing models to focus on the most relevant observations. It computes the similarity between queries ( $q$ ) and keys ( $k$ ), scaling by the key dimension to keep the gradients stable. Multihead Attention (MHA) (Vaswani et al., 2017) extends this by allowing the model to attend to different representation subspaces in parallel. Variants such as Sparse Attention (Zhang et al., 2021), BigBird (Zaheer et al., 2020), and Longformer (Beltagy et al., 2020) modify the attention pattern to reduce computational cost, particularly for long sequences, by attending only to selected positions rather than all pairs. Even with these improvements, the computation paths in these methods are discrete in nature, limiting their ability to model continuous trajectories often captured by their CT counterparts.

Recent work has explored bridging this gap through the Neural-ODE (Chen et al., 2018) formulation. mTAN (Shukla & Marlin, 2021) learns CT embeddings and uses time-based attention to interpolate irregular observations into a fixed-length representation for downstream encoder-decoder modeling. Continuous-time Attention (CTA) (Chien & Chen, 2021) embeds a CT-Attention mechanism within a Neural ODE, allowing attention weights and hidden states to evolve jointly over time. Nevertheless, it remains

computationally intensive and sensitive to the accuracy of the ODE solver. ODEFormer (d’Ascoli et al., 2023) trains a sequence-to-sequence transformer on synthetic trajectories to infer symbolic ODE systems directly from noisy, irregular data, although it struggles with chaotic systems and generalization beyond observed conditions. ContiFormer (Chen et al., 2023) builds a CT-Transformer by pairing ODE-defined latent trajectories with a time-aware attention mechanism to model dynamic relationships in data.

Despite these advancements, a persistent and underexplored gap remains in developing a biologically inspired attention mechanism that seamlessly integrates CT dynamics with the abstraction of the brain’s connectome. Building on this, we propose a novel attention mechanism called the *Neuronal Attention Circuit* (NAC), in which attention logits are computed as the solution to a first-order ODE modulated by nonlinear, interlinked gates derived from repurposing Neuronal Circuit Policies (NCPs) from the nervous system of *C.elegans* nematode (refer to Appendix A.1 for more information). Unlike standard attention, which projects key-query pairs through a dense layer, NAC employs a sensory gate to transform input features and a backbone network to model nonlinear interactions, with multiple heads producing outputs structured for attention logit computation. Based on the solutions to ODE, we define three computation modes: (i) Exact, using the closed-form ODE solution; (ii) Euler, approximating the solution via *explicit Euler* integration; and (iii) Steady, using only the steady-state solution, analogous to standard attention scores. To reduce computational complexity, we implement a sparse subquadratic Top- $K$  pairwise concatenation algorithm that selectively curates key-query inputs. We evaluate NAC across multiple domains, including irregularly sampled time-series, autonomous vehicle lane-keeping, and Industry 4.0, and compare it to state-of-the-art baselines. NAC consistently matches or outperforms these models, while runtime and peak memory benchmarks place it between CT-RNNs in terms of speed and CT-Attentions in terms of memory requirements. We also highlight the interpretability of NAC at the cell level.

## 2. Neuronal Attention Circuit (NAC)

We propose a simple alternative formulation of the attention logits  $a$  (refer to Appendix A.2 for more information), interpreting them as the solution to a first-order linear ODE modulated by nonlinear, interlinked gates:

$$\frac{da_t}{dt} = - \underbrace{f_{\omega_\tau}([\mathbf{q}; \mathbf{k}], t, \theta_{\omega_\tau})}_{\omega_\tau(\mathbf{u})} a_t + \underbrace{f_\phi([\mathbf{q}; \mathbf{k}], t, \theta_\phi)}_{\phi(\mathbf{u})}, \quad (1)$$

where  $\mathbf{u} = [\mathbf{q}; \mathbf{k}]$  denotes the sparse Top- $K$  concatenated query-key input.  $\omega_\tau$  represents a learnable time-constant gate head, and  $\phi$  denotes a nonlinear content-target head.

Both gates are parameterized by a backbone network derived from repurposing NCPs. We refer to this formulation as the Neuronal Attention Circuit (NAC). It enables the logit  $a_t$  to evolve dynamically with input dependent, variable time constants, mirroring the adaptive temporal dynamics found in *C.elegans* nervous systems while improving computational efficiency and expressiveness. Moreover, it introduces continuous depth into the attention mechanism, bridging discrete-layer computation with dynamic temporal evolution.

**Motivation behind this formulation:** The proposed formulation is loosely motivated by the input-dependent time-constant mechanism of LNNs, a class of CT-RNNs inspired by biological nervous systems and synaptic transmission. In this framework, the dynamics of nonspiking neurons are described by a linear ODE with nonlinear, interlinked gates:  $\frac{dx_t}{dt} = \frac{x_t}{\tau} + \mathbf{S}_t$ , where  $\mathbf{x}_t$  denotes the hidden state and where  $\mathbf{S}_t \in \mathbb{R}^M$  represents a nonlinear contribution defined as  $f(\mathbf{x}_t, \mathbf{u}, t, \theta)(A - \mathbf{x}_t)$ . Here,  $A$  and  $\theta$  are learnable parameters. Plugging  $\mathbf{S}_t$  yields  $\frac{dx_t}{dt} = -[\frac{1}{\tau} + f(\mathbf{x}_t, \mathbf{u}, t, \theta)] \mathbf{x}_t + f(\mathbf{x}_t, \mathbf{u}, t, \theta)A$ . LNNs are known for their strong expressivity, stability, and performance in irregularly sampled time-series modeling (Hasani et al., 2021; 2022).

**NAC’s forward-pass update using ODE solver:** The state of NAC at time  $t$  can be computed using a numerical ODE solver that simulates the dynamics from an initial state  $a_0$  to  $a_t$ . The solver discretizes the continuous interval  $[0, T]$  into steps  $[t_0, t_1, t_2, \dots, t_n]$ , with each step updating the state from  $t_i$  to  $t_{i+1}$ . For our purposes, we use the *explicit Euler* solver, which is simple, efficient, and easy to implement. Although methods such as Runge-Kutta may offer higher accuracy, their computational overhead makes them less suitable for large-scale neural simulations that require numerous updates, especially since the logits are normalized, and exact precision is not necessary. Let the step size be  $\Delta t$ , with discrete times  $t_n = n\Delta t$  and logit states  $a_n = a(t_n)$ . Using the *explicit Euler* method, the update is

$$a_{n+1} = a_n + \Delta t (-\omega_\tau a_n + \phi). \quad (2)$$

**Closed-form (Exact) Computation of NAC:** We now derive the analytical solution for Eqn. 1. The gates  $\phi$  and  $\omega_\tau$  are time-varying and depend on the input sequence at each time step. However, to enable an efficient closed-form forward-pass update, we apply a piecewise constant assumption (locally frozen-coefficient approximation (John, 1952)) over a small interval. Under this assumption, with initial condition  $a_0$ , the analytical closed-form solution is as follows:

$$a_t = \underbrace{a^*}_{\text{steady-state}} + \underbrace{(a_0 - a^*) e^{-\omega_\tau t}}_{\text{transient}} \quad (3)$$

Here,  $a^* = \phi/\omega_\tau$  is the steady-state solution. The detailed derivation and analysis are provided in Appendix B.1.

## 2.1. Stability Analysis of NAC

We now investigate the stability bounds of *NAC* under both the ODE-based and the Closed-Form formulations.

### 2.1.1. STATE STABILITY

We analyze state stability in both single-connection and multi-connection settings. This analysis establishes the boundness of the attention logit state trajectory, ensuring that, under positive decay rates, the dynamics remain well-behaved without divergence or overshoot.

**Theorem 1** (State Stability). *Let  $a_t^{(i)}$  denote the state of the  $i$ -th attention logit governed by  $da_t^{(i)}/dt = -\omega_\tau a_t^{(i)} + \phi$ . Assume that  $\phi$  and  $\omega_\tau$  decompose across  $M$  incoming connections as  $\phi = \sum_{j=1}^M f_\phi([\mathbf{q}_i; \mathbf{k}_j])$ , and  $\omega_\tau = \sum_{j=1}^M f_{\omega_\tau}([\mathbf{q}_i; \mathbf{k}_j])$ , with  $f_{\omega_\tau} > 0$ . Define the per-connection equilibrium  $A_{i,j} = f_\phi([\mathbf{q}_i; \mathbf{k}_j])/f_{\omega_\tau}([\mathbf{q}_i; \mathbf{k}_j])$ , and let  $A_i^{\min} = \min_j A_{i,j}$  and  $A_i^{\max} = \max_j A_{i,j}$ . Then for any finite horizon  $t \in [0, T]$ , the state trajectory satisfies*

$$\min(0, A_i^{\min}) \leq a_t^{(i)} \leq \max(0, A_i^{\max}), \quad (4)$$

provided the initial condition  $a_i(0)$  lies within this range. In the special case of a single connection ( $M = 1$ ), the bounds collapse to

$$\min(0, A_i) \leq a_t^{(i)} \leq \max(0, A_i), \quad (5)$$

where  $A_i = f_\phi/\omega_\tau$  is exactly the steady-state solution from Eqn. 3. The proof is provided in the Appendix B.2.

### 2.1.2. CLOSED-FORM ERROR & EXPONENTIAL BOUNDS

We now examine the asymptotic stability, error characterization, and exponential boundedness of the closed-form formulation. We begin by quantifying the deviation of the trajectory from its steady-state solution. Define the instantaneous error

$$\varepsilon_t = a_t - a^*, \quad (6)$$

which measures the distance of the system state to equilibrium at time  $t$ . From Eqn. 3, the error admits the exact representation

$$\varepsilon_t = (a_0 - a^*)e^{-\omega_\tau t} \quad (7)$$

In particular, the pointwise absolute error is given by

$$|\varepsilon_t| = |a_0 - a^*| e^{-\omega_\tau t} \quad (8)$$

This reveals that convergence is not merely asymptotic but follows an exact exponential law, controlled by the rate parameter  $\omega_\tau$ . This yields the following finite-time guarantee.

**Corollary 1** (Exponential decay bound). *If  $\omega_\tau > 0$ , then for all  $t \geq 0$ ,*

$$|a_t - a^*| \leq |a_0 - a^*| e^{-\omega_\tau t}. \quad (9)$$

*Remark:* If  $\omega_\tau > 0$  then  $\lim_{t \rightarrow \infty} e^{-\omega_\tau t} = 0$ , therefore  $a_t \rightarrow a^*$ . The convergence is exponential with rate  $\omega_\tau$ . If  $\omega_\tau < 0$  then  $e^{-\omega_\tau t} = e^{|\omega_\tau|t}$  diverges so that  $a_t$  grows exponentially away from  $a^*$  in magnitude (unless initial offset  $a_0 - a^* = 0$ , a measure-zero case). If  $\omega_\tau = 0$  the ODE is  $\dot{a} = \phi$  and the solution is linear in  $t$  (unless  $\phi = 0$ ). For bounded dynamics that converge to an interpretable steady-state, it is required that  $\omega_\tau > 0$ .

**Corollary 2** (Uniform initialization). *If the initialization is known only to belong to a bounded set, i.e.,  $|a_0 - a^*| \leq M$  for some  $M > 0$ , then the error admits the uniform bound*

$$|a_t - a^*| \leq M e^{-\omega_\tau t}. \quad (10)$$

*Remark:* This bound highlights that exponential convergence holds uniformly across all admissible initial conditions, with the constant  $M$  capturing the worst-case deviation.

**Corollary 3** (Sample complexity to  $\delta$ -accuracy). *A natural operational question is the time required to achieve a target tolerance  $\delta > 0$ . Solving*

$$|a_0 - a^*| e^{-\omega_\tau t} \leq \delta, \quad (11)$$

We obtain the threshold

$$t \geq \frac{1}{\omega_\tau} \ln \frac{|a_0 - a^*|}{\delta}. \quad (12)$$

*Remark:* The convergence rate is inversely proportional to  $\omega_\tau$ , and the required time scales only logarithmically at the accuracy level  $1/\delta$ . Intuitively, a larger  $\omega_\tau$  accelerates contraction toward equilibrium, yielding faster attainment of any prescribed tolerance.

## 2.2. Designing the Neural Network

We now outline the design of a neural network layer guided by the preceding analysis. The process involves five steps: (i) repurposing NCPs; (ii) input curation; (iii) construction of the time vector ( $t$ ); (iv) computing attention logits and weights; and (v) generating the attention output. Figure 2 provides a graphical overview of NAC.

**Repurposing NCPs:** We repurpose the NCPs framework by converting its fixed, biologically derived wiring (see Figure 1(a)) into a flexible recurrent architecture that allows configurable input–output mappings. Instead of enforcing

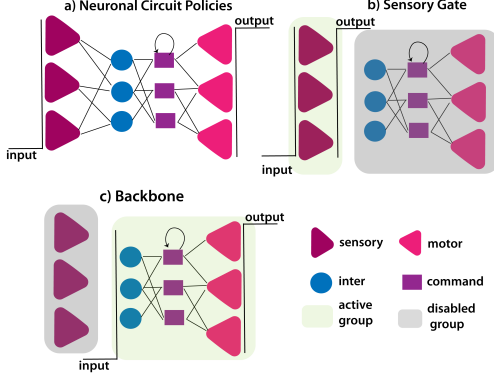


Figure 1. Illustration of (a) NCPs with predetermined wiring; (b) Sensory gate, where sensory neurons are active, and the remaining neurons are disabled for the  $q$ ,  $k$ , and  $v$  projections; (c) Backbone, showing inter-motor projections with sensory neurons disabled in extended heads for computing  $\phi$  and  $\omega_\tau$ .

### Algorithm 1 Repurposed NCPCell

**Require:** Wiring  $\mathcal{W}$  with  $(A_{\text{in}}, A_{\text{rec}})$ , groups  $(N_s, N_i, N_c, N_m)$ , activation  $\alpha$ , input group  $G_{\text{input}}$ , output group  $G_{\text{output}}$ , disabled groups  $\mathcal{D}$   
**Ensure:** Output  $y_t \in \mathbb{R}^{B \times d_{\text{out}}}$ , state  $\mathbf{x}_t \in \mathbb{R}^{B \times d_h}$   
 Binary mask:  $M_{\text{rec}} \leftarrow |A_{\text{rec}}|$ ,  $M_{\text{in}} \leftarrow |A_{\text{in}}|$   
 Initialize parameters:  $W_{\text{in}}, W_{\text{rec}}, b, w_{\text{in}}, b_{\text{in}}, w_{\text{out}}, b_{\text{out}}$   
 Input neurons:  $I_{\text{in}} \leftarrow G_{\text{input}}$   
 Output neurons:  $I_{\text{out}} \leftarrow G_{\text{output}}$   
 Define activation mask:  $\text{mask}_{\text{act},i} = 0$  if  $i \in \mathcal{D}$  else 1  
 Input Projections:  $\tilde{u}_t \leftarrow u_t \odot w_{\text{in}} + b_{\text{in}}$   
 Recurrent computation:  $r_t \leftarrow \mathbf{x}_{t-1} (W_{\text{rec}} \odot M_{\text{rec}})$   
 Sparse computation:  $s_t \leftarrow \tilde{u}_t (W_{\text{in}} \odot M_{\text{in}})$   
 Neuron update:  $\mathbf{x}_t \leftarrow \alpha(r_t + s_t + b) \odot \text{mask}_{\text{act}}$   
 Output mapping:  $y_t \leftarrow (\mathbf{x}_t[I_{\text{out}}] \odot w_{\text{out}}) + b_{\text{out}}$   
**return**  $(y_t, \mathbf{x}_t)$

a static connectome, our approach exposes adjacency matrices as modifiable structures defining sparse input and recurrent connections. This enables selective information routing across neuron groups while retaining the original circuit topology. Decoupling wiring specifications from model instantiation allows dynamic connectivity adjustments to accommodate different input modalities without full retraining. Algorithm 1 summarizes the steps for repurposing the NCPs wiring mechanism. Key features include groupwise masking for neuron isolation, adaptive remapping of inputs and outputs for task-specific adaptation, and tunable sparsity  $s$  to balance expressiveness and efficiency.

In our implementation, the sensory neuron gate ( $\mathcal{NN}_{\text{sensory}}$ ) projects the  $q$ ,  $k$ , and  $v$  representations (see Figure 1(b)). This enables sensory neurons to maintain structured, context-aware representations rather than collapsing inputs into fully connected layers. As a result, the network preserves locality and modularity, which improves information routing. Intuitively, it acts like biological receptor neurons, converting external stimulus inputs into organized signals that feed into

### Algorithm 2 Sparse Top- $K$ Pairwise Concatenation

**Require:** Queries  $Q \in \mathbb{R}^{B \times H \times T_q \times D}$ , Keys  $K \in \mathbb{R}^{B \times H \times T_k \times D}$ , Top- $K$  value  $K$   
**Ensure:** Concatenated tensor  $U \in \mathbb{R}^{B \times H \times T_q \times K_{\text{eff}} \times 2D}$   
 Block Size:  $B_s \leftarrow \lfloor \sqrt{T_k} \rfloor$   
 Partition  $K$  into  $N_b$  blocks:  $K_{\text{blocks}} \in \mathbb{R}^{B \times H \times N_b \times B_s \times D}$   
 Block Centroids:  $\bar{K} \leftarrow \text{mean}(K_{\text{blocks}})$   
 Coarse Scores:  $S_{\text{coarse}} \leftarrow Q \cdot \bar{K}^\top$   
 Select Top- $M$  Blocks:  $I_{\text{blocks}} \leftarrow \text{top\_k}(S_{\text{coarse}}, \lceil K/B_s \rceil)$   
 Gather Candidates:  $K_{\text{cand}} \leftarrow \text{gather}(K_{\text{blocks}}, I_{\text{blocks}})$   
 Fine Scores:  $S_{\text{fine}} \leftarrow \text{reduce\_sum}(Q \odot K_{\text{cand}})$   
 Effective Top- $K$ :  $K_{\text{eff}} \leftarrow \min(K, \text{size}(K_{\text{cand}}))$   
 Indices:  $I_{\text{topk}} \leftarrow \text{top\_k}(S_{\text{fine}}, K_{\text{eff}})$   
 Selected Keys:  $K_{\text{selected}} \leftarrow \text{gather}(K_{\text{cand}}, I_{\text{topk}})$   
 Concatenate:  $U_{\text{topk}} \leftarrow [Q; K_{\text{selected}}] \in \mathbb{R}^{B \times H \times T_q \times K_{\text{eff}} \times 2D}$   
**return**  $U_{\text{topk}}$

downstream circuits.

$$\begin{aligned} \mathcal{NN}_{\text{sensory}} &= \text{NCPCell}(G_{\text{input}} = [N_s], \\ &G_{\text{output}} = [N_s], \mathcal{D} = [N_i, N_c, N_m], s) \end{aligned} \quad (13)$$

The inter-to-motor pathways form a backbone network ( $\mathcal{NN}_{\text{backbone}}$ ) with branches that compute  $\phi$  and  $\omega_\tau$  (see Figure 1(c)). Intuitively, this integrates neuronal activity over time and produces outputs that regulate gating signals. Instead of learning  $\phi$  and  $\omega_\tau$  independently, this backbone allows the model to learn shared representations, enabling multiple benefits: (i) separate head layers enable the system to capture temporal and structural dependencies independently; (ii) accelerates convergence during training.

$$\begin{aligned} \mathcal{NN}_{\text{backbone}} &= \text{NCPCell}(G_{\text{input}} = [N_i], \\ &G_{\text{output}} = [N_m], \mathcal{D} = [N_s], s) \end{aligned} \quad (14)$$

The output heads are defined as:

$$\phi = \sigma(\mathcal{NN}_{\text{backbone}}(\mathbf{u})) \quad (15)$$

$$\omega_\tau = \text{softplus}(\mathcal{NN}_{\text{backbone}}(\mathbf{u})) + \varepsilon, \quad \varepsilon > 0 \quad (16)$$

Here,  $\phi$  serves as a *content-target gate* head, where the sigmoid function  $\sigma(\cdot)$  determines the target signal strength. In contrast,  $\omega_\tau$  is a strictly positive *time-constant gate* head that controls the rate of convergence and the steady-state amplitude. Conceptually, this parallels recurrent gating:  $\phi$  regulates *what* content to emphasize, while  $\omega_\tau$  governs *how quickly* and *to what extent* it is expressed.

**Input Curation:** Initially, full pairwise concatenation was used to form a joint tensor  $U \in \mathbb{R}^{B \times H \times T_q \times T_k \times 2D}$  from  $Q \in \mathbb{R}^{B \times H \times T_q \times D}$  and  $K \in \mathbb{R}^{B \times H \times T_k \times D}$ . However, this approach becomes computationally intractable as the sequence length increases, leading to  $\mathcal{O}(n^2)$  memory growth, severe memory fragmentation, and frequent hardware memory exhaustion. A naive sparse Top- $K$  pruning strategy

was then implemented to reduce the load on subsequent layers. While this reduced downstream computation, it failed to address the fundamental quadratic bottleneck in the initial scoring and storage stages, rendering the optimization ineffective for long sequences. To mitigate this issue, we then implemented a subquadratic Top- $K$  selection strategy based on square-root partitioning (Child et al., 2019). By dynamically segmenting the key sequence into blocks and scoring queries against block centroids, the method identifies high-salience candidate regions without ever materializing the full  $T_q \times T_k$  matrix. This hierarchical approach reduces the scoring complexity to  $\mathcal{O}(n\sqrt{n})$ , producing a sparse tensor  $U_{\text{topk}}$  that enables linear memory scaling in subsequent backbone layers. The mechanism is self-adaptive and eliminates the need for manual block-size tuning (Algorithm 2). The efficiency and complexity comparison is provided in Appendix C.2.

**Construction of Time Vector ( $t$ ):** NAC builds on continuous-depth models as in (Hasani et al., 2022), which adapt their temporal dynamics to the task. It constructs an internal, normalized time vector  $t = \sigma(t_a \cdot t_{\text{sample}} + t_b) \in [0, T]$ , where  $t_a$  and  $t_b$  are learnable affine parameters (computed per query-key pair) and  $\sigma$  is the sigmoid function. For time-varying datasets (e.g., irregularly sampled series), each  $t_{\text{sample}}$  is derived from the sample’s timestamp, enabling time-dependent modulation of attention dynamics. For tasks without meaningful timing,  $t_{\text{sample}}$  is set to 1, resulting in  $t = \sigma(t_a + t_b) \in [0, 1]$ , providing a smooth, bounded representation of  $t$  for modulating the network’s dynamics.

**Attention logits and weights:** Starting from Eqn. 3, consider the trajectory of a query–key pair with initial condition  $a_0 = 0$ :

$$a_t = \frac{\phi}{\omega_\tau} (1 - e^{-\omega_\tau t}), \quad (17)$$

For finite  $t_{\text{sample}}$ , the exponential factor  $(1 - e^{-\omega_\tau t})$  regulates the buildup of attention, giving  $\omega_\tau$  a temporal gating role. Normalizing across all keys via *softmax* yields attention weights  $\alpha_t = \text{softmax}(a_t)$ , defining a valid probability distribution where  $\phi$  amplifies or suppresses content alignments, and  $\omega_\tau$  shapes both the speed and saturation of these preferences.

As  $t_{\text{sample}} \rightarrow \infty$ , the trajectory converges to the steady state

$$a_t^* = \frac{\phi}{\omega_\tau}, \quad (18)$$

which we introduce as a computation mode. Conceptually, it is analogous to scaled-dot attention: it aggregates information across inputs in a similar form, even though  $\phi$  cannot reproduce exact dot products.

**Attention output:** Finally, the attention output is computed by integrating the  $\alpha_t$  with the  $v_t$  matrix over internally con-

structed time-window  $t$ :

$$\text{NAC}(q, k, v) = \int_T \alpha_t v_t dt \quad (19)$$

Intuitively, this integral acts as a continuous aggregator of the  $v_t$ , where each contribution is weighted by its instantaneous relevance. In practice, we approximate it via a time-modulated sum:  $\sum_i \alpha_t^{(i)} v_t^{(i)} t^{(i)}$  where  $t^{(i)}$  serves as a flexible quadrature weight that adaptively scales the contribution of each time-step, complementing  $\alpha_t^{(i)}$ . This parameterization allows the model to modulate temporal contributions independently of semantic alignment while preserving differentiability and maintaining the original value representations.

### 2.2.1. EXTENSION TO MULTIHEAD

To scale this mechanism to multihead setting, we project the input sequence into  $H$  independent subspaces (heads) of dimension  $d_{\text{model}}/H$ , yielding query, key, and value tensors  $(q^{(h)}, k^{(h)}, v^{(h)})$  for  $h \in \{1, \dots, H\}$ . For each head, pairwise logits are computed according to Eqns. 2,3 or 18, followed by *Softmax* normalization to calculate attention weights. The resulting attention weights  $\alpha_t^{(h)}$  are then integrated with the value vector  $v^{(h)}$ , to produce head-specific attention outputs. Finally, these outputs are concatenated and linearly projected back into the model dimension. This formulation ensures that each head learns distinct dynamic compatibilities governed by its own parameterization of  $\phi$  and  $\omega_\tau$ , aggregation across heads preserves the expressive capacity of the standard multihead attention mechanism.

### 2.3. NAC as Universal Approximator

We now establish the universal approximation capability of NAC by extending the classical Universal Approximation Theorem (UAT) (Nishijima, 2021) to the proposed mechanism. For brevity, we consider a network with a single NAC layer processing fixed-dimensional inputs, although the argument generalizes to sequences.

**Theorem 2** (Universal Approximation by NAC). *Let  $K \subset \mathbb{R}^n$  be a compact set and  $f : K \rightarrow \mathbb{R}^m$  be a continuous function. For any  $\epsilon > 0$ , there exists a neural network consisting of a single NAC layer, with a sufficiently large model dimension  $d_{\text{model}}$ , number of heads  $H$ , sparsity  $s$ , and nonlinear activations, such that the network’s output  $g : \mathbb{R}^n \rightarrow \mathbb{R}^m$  satisfies*

$$\sup_{x \in K} \|f(x) - g(x)\| < \epsilon. \quad (20)$$

*The proof is provided in Appendix B.3.*

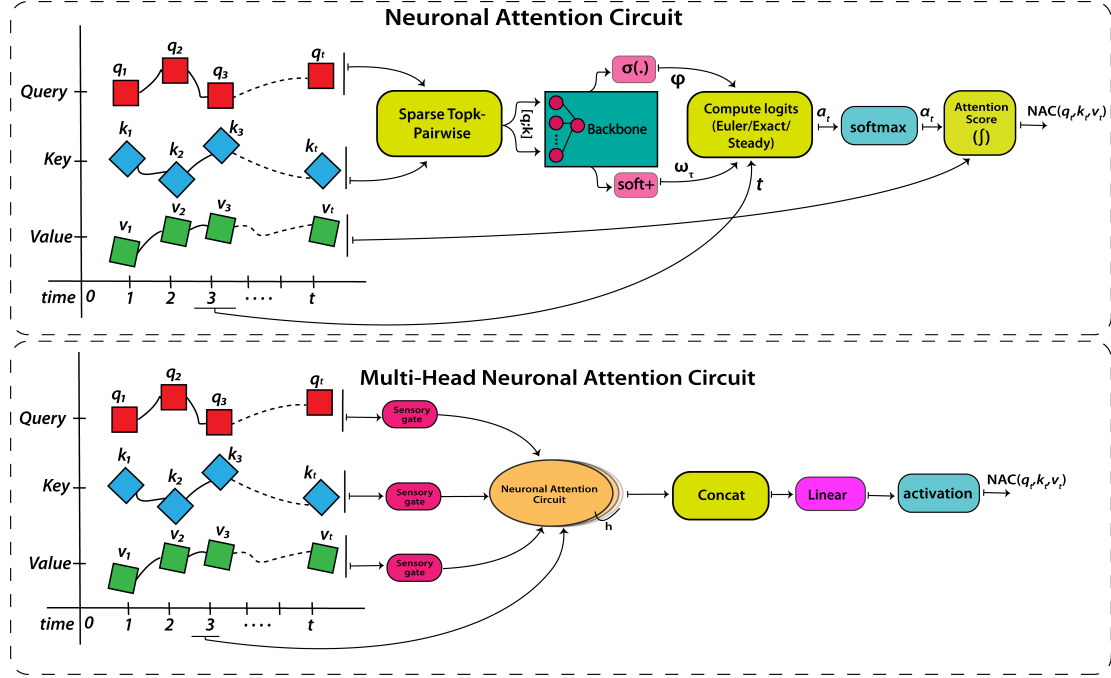


Figure 2. Illustration of the architecture of (a) Neuronal Attention Circuit mechanism ; (b) Multi-Head Extension

### 3. Evaluation

We evaluate the proposed architecture against a range of baselines, including (DT & CT) RNNs, (DT & CT) Attentions, and multiple NAC ablation configurations. Experiments are conducted across diverse domains, including irregular time-series modeling, the lane keeping of autonomous vehicles, and Industry 4.0 prognostics. All the results are obtained using 5-fold cross-validation, where the models are trained using BPTT (see Appendix C.3) on each fold and evaluated across all the folds. We report the mean ( $\mu$ ) and standard deviation ( $\sigma$ ) to capture variability and quantify uncertainty in the predictions. Table 1 provides the results for all the experiments, and the details of the baselines, ablations, environments, data, preprocessing, and neural network architectures for all the experiments are provided in Appendix D.3.

#### 3.1. Irregular time-series

We evaluate the proposed architecture on two irregular time-series datasets: (i) Event-based MNIST; and (ii) Person Activity Recognition (PAR).

**Event-based MNIST:** Event-based MNIST is the transformation of the widely recognized MNIST dataset with irregular sampling added originally proposed in (Lechner & Hasani, 2022). The transformation was performed in two steps: (i) flattening each  $28 \times 28$  image into a time-series of length 784 and (ii) encoding the binary time-series into an event-based format by collapsing consecutive identical

values (e.g., 1,1,1,1  $\rightarrow$  (1, t=4)). This representation requires models to handle temporal dependencies effectively. NAC-PW achieves an accuracy of 96.64%, followed by NAC-Exact/05s/8k at 96.12%. GRU-ODE and ContiFormer ranked third with 96.04%.

**Person Activity Recognition (PAR):** We employed the Localized Person Activity dataset from UC Irvine (Vidulin et al., 2010). The dataset contains data from five participants, each equipped with inertial measurement sensors sampled every 211 ms. The goal of this experiment is to predict a person’s activity from a set of predefined actions, making it a classification task. All models performed well on this task, with NAC-PW achieving 90.18% accuracy and taking first place. NAC-Exact/05s/8k ranked second with 90.11% accuracy, while NAC-Steady ranked third with 89.79% mean accuracy.

#### 3.2. Lane Keeping of Autonomous Vehicles

Lane keeping in autonomous vehicles (AVs) is a fundamental problem in robotics and AI. Early works (Tiang et al., 2018) focused primarily on accuracy, often relying on large models. More recent research (Lechner et al., 2020; Razzaq & Hongwei, 2023) has shifted toward designing compact architectures suitable for resource-constrained devices. The goal of this experiment is to create a long structure between the road’s horizon and the corresponding steering commands. For evaluation, we used two widely adopted simulation environments: (i) OpenAI CarRacing (Brockman et al., 2016); and (ii) the Udacity Self-Driving Car Simu-

Table 1. Model Performance across all categories and datasets

| Model              | Irregular Time-Series            |                                  | Lane-Keeping of AVs              |                                     | Industry 4.0                     |                                  |                                  |
|--------------------|----------------------------------|----------------------------------|----------------------------------|-------------------------------------|----------------------------------|----------------------------------|----------------------------------|
|                    | E-MNIST ( $\uparrow$ )           | PAR ( $\uparrow$ )               | CarRacing ( $\uparrow$ )         | Udacity ( $\downarrow$ )            | PRONOSTIA ( $\downarrow$ )       | XJTU-SY ( $\downarrow$ )         | HUST ( $\downarrow$ )            |
| RNN                | 95.59 $\pm$ 0.37                 | 88.77 $\pm$ 0.58                 | 78.90 $\pm$ 3.35                 | 0.0210 $\pm$ 0.0014                 | 42.05 $\pm$ 7.49                 | 31.07 $\pm$ 6.63                 | 42.22 $\pm$ 8.16                 |
| LSTM               | 95.88 $\pm$ 0.23                 | 88.36 $\pm$ 0.79                 | 80.60 $\pm$ 0.12                 | 0.0181 $\pm$ 0.0014                 | 41.87 $\pm$ 2.88                 | 31.99 $\pm$ 8.32                 | 44.09 $\pm$ 2.14                 |
| GRU                | 95.85 $\pm$ 0.22                 | 88.68 $\pm$ 1.35                 | 80.60 $\pm$ 0.22                 | 0.0206 $\pm$ 0.0014                 | 44.22 $\pm$ 4.60                 | 26.65 $\pm$ 4.49                 | 41.86 $\pm$ 7.96                 |
| CT-RNN             | 95.18 $\pm$ 0.20                 | 88.71 $\pm$ 0.87                 | 80.21 $\pm$ 0.27                 | 0.0206 $\pm$ 0.0013                 | 44.32 $\pm$ 8.69                 | 26.01 $\pm$ 8.74                 | 39.99 $\pm$ 6.33                 |
| GRU-ODE            | <b>96.04<math>\pm</math>0.13</b> | 89.01 $\pm$ 1.55                 | 80.29 $\pm$ 0.72                 | 0.0188 $\pm$ 0.0016                 | 45.11 $\pm$ 3.19                 | 31.20 $\pm$ 8.69                 | 43.91 $\pm$ 7.10                 |
| PhasedLSTM         | 95.79 $\pm$ 0.14                 | 88.93 $\pm$ 1.08                 | 80.35 $\pm$ 0.38                 | 0.0186 $\pm$ 0.0015                 | 44.15 $\pm$ 4.80                 | 35.49 $\pm$ 5.54                 | 38.66 $\pm$ 5.55                 |
| mmRNN              | 95.74 $\pm$ 0.27                 | 88.48 $\pm$ 0.46                 | 80.13 $\pm$ 0.54                 | 0.0205 $\pm$ 0.0027                 | 48.50 $\pm$ 4.60                 | 27.84 $\pm$ 4.05                 | 40.11 $\pm$ 9.56                 |
| LTC                | 95.25 $\pm$ 0.00                 | 88.12 $\pm$ 0.68                 | 76.37 $\pm$ 3.01                 | 0.0245 $\pm$ 0.0024                 | 48.14 $\pm$ 5.01                 | 36.83 $\pm$ 8.57                 | 61.82 $\pm$ 15.64                |
| CfC                | 94.16 $\pm$ 0.49                 | 88.60 $\pm$ 0.34                 | 80.59 $\pm$ 0.33                 | 0.0198 $\pm$ 0.0022                 | 47.78 $\pm$ 3.54                 | 35.51 $\pm$ 3.94                 | 54.09 $\pm$ 10.13                |
| DeepState          | 96.01 $\pm$ 0.07                 | 86.25 $\pm$ 0.62                 | 80.25 $\pm$ 0.20                 | 0.0175 $\pm$ 0.0007                 | 40.86 $\pm$ 4.45                 | 30.42 $\pm$ 5.24                 | 40.88 $\pm$ 2.11                 |
| S4                 | 95.21 $\pm$ 0.07                 | 89.68 $\pm$ 0.84                 | 80.32 $\pm$ 0.68                 | 0.0183 $\pm$ 0.0010                 | 669.68 $\pm$ 337.38              | 339.49 $\pm$ 155.48              | 533.19 $\pm$ 232.99              |
| Attention          | 95.68 $\pm$ 0.23                 | 88.29 $\pm$ 0.98                 | 80.40 $\pm$ 0.26                 | 0.0193 $\pm$ 0.0009                 | 41.89 $\pm$ 6.98                 | 26.29 $\pm$ 4.06                 | 40.28 $\pm$ 4.23                 |
| MHA                | 95.94 $\pm$ 0.15                 | 88.36 $\pm$ 1.06                 | 79.99 $\pm$ 0.49                 | 0.0185 $\pm$ 0.0017                 | 45.36 $\pm$ 5.16                 | 37.31 $\pm$ 12.20                | 41.40 $\pm$ 7.72                 |
| Linear Attention   | 95.87 $\pm$ 0.14                 | 88.75 $\pm$ 0.85                 | 80.16 $\pm$ 0.30                 | 0.0196 $\pm$ 0.0015                 | 58.35 $\pm$ 8.67                 | 87.80 $\pm$ 19.52                | 99.38 $\pm$ 37.47                |
| Performer          | 96.01 $\pm$ 0.18                 | 88.71 $\pm$ 1.06                 | 80.11 $\pm$ 0.39                 | 0.0180 $\pm$ 0.0007                 | 45.37 $\pm$ 4.51                 | 38.05 $\pm$ 5.75                 | 39.06 $\pm$ 7.23                 |
| mTAN               | 95.97 $\pm$ 0.25                 | 88.08 $\pm$ 0.94                 | 80.86 $\pm$ 0.22                 | 0.0178 $\pm$ 0.0005                 | 44.41 $\pm$ 7.15                 | 41.34 $\pm$ 3.72                 | 66.29 $\pm$ 4.25                 |
| CTA                | 95.86 $\pm$ 0.14                 | 88.10 $\pm$ 1.10                 | 80.54 $\pm$ 0.40                 | 0.0197 $\pm$ 0.0016                 | 39.16 $\pm$ 3.54                 | <b>25.86<math>\pm</math>1.47</b> | 38.41 $\pm$ 4.51                 |
| ODEFormer          | 95.62 $\pm$ 0.20                 | 88.25 $\pm$ 0.66                 | 80.54 $\pm$ 0.40                 | 0.0190 $\pm$ 0.0012                 | 42.42 $\pm$ 6.98                 | 35.63 $\pm$ 9.24                 | 40.60 $\pm$ 6.83                 |
| ContiFormer        | <b>96.04<math>\pm</math>0.23</b> | 81.28 $\pm$ 0.85                 | 80.47 $\pm$ 0.50                 | <b>0.0174<math>\pm</math>0.0013</b> | <b>37.82<math>\pm</math>7.09</b> | 34.71 $\pm$ 4.98                 | 43.81 $\pm$ 10.18                |
| NAC-2k             | 95.73 $\pm$ 0.07                 | 89.70 $\pm$ 0.98                 | 80.59 $\pm$ 0.46                 | 0.0208 $\pm$ 0.0015                 | 43.78 $\pm$ 2.71                 | 37.43 $\pm$ 9.28                 | 40.51 $\pm$ 6.61                 |
| NAC-32k            | 95.15 $\pm$ 0.11                 | 89.44 $\pm$ 0.87                 | 80.38 $\pm$ 0.16                 | <b>0.0170<math>\pm</math>0.0007</b> | 49.53 $\pm$ 4.89                 | 32.45 $\pm$ 10.84                | 39.17 $\pm$ 12.23                |
| NAC-PW             | <b>96.64<math>\pm</math>0.12</b> | <b>90.18<math>\pm</math>1.01</b> | <b>80.72<math>\pm</math>0.41</b> | 0.0177 $\pm$ 0.0008                 | <b>37.50<math>\pm</math>2.56</b> | 28.01 $\pm$ 4.93                 | <b>30.14<math>\pm</math>6.87</b> |
| NAC-09s            | 95.86 $\pm$ 0.11                 | 89.76 $\pm$ 0.65                 | 80.43 $\pm$ 0.17                 | 0.0188 $\pm$ 0.0013                 | 47.29 $\pm$ 5.52                 | 40.40 $\pm$ 8.85                 | 44.39 $\pm$ 6.82                 |
| NAC-02s            | 95.51 $\pm$ 0.06                 | 89.47 $\pm$ 1.38                 | 80.47 $\pm$ 0.27                 | 0.0188 $\pm$ 0.0013                 | 39.43 $\pm$ 5.94                 | 35.59 $\pm$ 3.86                 | 38.90 $\pm$ 6.43                 |
| NAC- $\phi$ linear | 95.89 $\pm$ 0.22                 | 89.73 $\pm$ 0.89                 | 80.58 $\pm$ 0.24                 | 0.0184 $\pm$ 0.0024                 | 42.64 $\pm$ 3.68                 | <b>29.53<math>\pm</math>4.49</b> | <b>35.89<math>\pm</math>7.08</b> |
| NAC- $\phi$ tanh   | 95.70 $\pm$ 0.32                 | 89.67 $\pm$ 1.27                 | 80.60 $\pm$ 0.06                 | 0.0175 $\pm$ 0.0016                 | 45.99 $\pm$ 4.55                 | 33.99 $\pm$ 3.96                 | 38.75 $\pm$ 9.69                 |
| NAC-FC             | 95.31 $\pm$ 0.07                 | 88.48 $\pm$ 1.24                 | 80.49 $\pm$ 0.46                 | 0.0183 $\pm$ 0.0017                 | 47.89 $\pm$ 5.16                 | 41.94 $\pm$ 9.37                 | 46.25 $\pm$ 6.83                 |
| NAC-09sFC          | 95.24 $\pm$ 0.05                 | 88.13 $\pm$ 1.00                 | 80.51 $\pm$ 0.35                 | 0.0251 $\pm$ 0.0040                 | 378.20 $\pm$ 110.33              | 157.15 $\pm$ 31.49               | 315.32 $\pm$ 65.92               |
| NAC-05sFC          | 95.13 $\pm$ 0.14                 | 88.23 $\pm$ 1.44                 | 75.99 $\pm$ 8.81                 | 0.0263 $\pm$ 0.0039                 | 404.28 $\pm$ 105.84              | 154.89 $\pm$ 55.80               | 272.90 $\pm$ 74.83               |
| NAC-02sFC          | 95.06 $\pm$ 0.47                 | 87.88 $\pm$ 1.21                 | 80.17 $\pm$ 0.48                 | 0.0251 $\pm$ 0.0020                 | 233.34 $\pm$ 95.27               | 150.06 $\pm$ 57.33               | 317.89 $\pm$ 104.40              |
| NAC-Exact/05s/8k   | <b>96.12<math>\pm</math>0.11</b> | <b>90.11<math>\pm</math>0.79</b> | 80.59 $\pm$ 1.82                 | <b>0.0173<math>\pm</math>0.0006</b> | <b>37.75<math>\pm</math>4.72</b> | <b>22.87<math>\pm</math>1.75</b> | <b>27.82<math>\pm</math>7.09</b> |
| NAC-Euler          | 95.67 $\pm$ 0.26                 | 89.70 $\pm$ 1.54                 | <b>80.61<math>\pm</math>0.28</b> | 0.0181 $\pm$ 0.0017                 | 42.08 $\pm$ 6.14                 | 28.46 $\pm$ 8.18                 | 39.32 $\pm$ 9.15                 |
| NAC-Steady         | 95.75 $\pm$ 0.28                 | <b>89.79<math>\pm</math>1.67</b> | <b>80.62<math>\pm</math>0.26</b> | 0.0181 $\pm$ 0.0012                 | 40.95 $\pm$ 5.77                 | 26.76 $\pm$ 7.36                 | 37.12 $\pm$ 12.43                |

Note: ( $\uparrow$ ) higher is better; ( $\downarrow$ ) lower is better.

lator (uda). In OpenAI CarRacing, the task is to classify steering actions from a predefined action set. In contrast, the Udacity Simulator requires the prediction of a continuous trajectory of steering values. We implemented the AI models proposed by (Razzaq & Hongwei, 2023), replacing the recurrent layer with NAC and its counterparts. All models achieved approximately 80% accuracy on average in the OpenAI CarRacing benchmark. Notably, the NAC-PW performed the best, reaching the highest accuracy of 80.72%, followed by NAC-Steady, ranked second with 80.62%. LSTM and GRU take third position, achieving 80.60% on average. For the Udacity benchmark, NAC-32k performed the best, achieving the lowest MSE of 0.0170. NAC-Exact/05s/8k followed by 0.0173, and ContiFormer ranked third with 0.0174. Experimental videos are available for the OpenAI CarRacing [click here] and for the Udacity Simulator [click here].

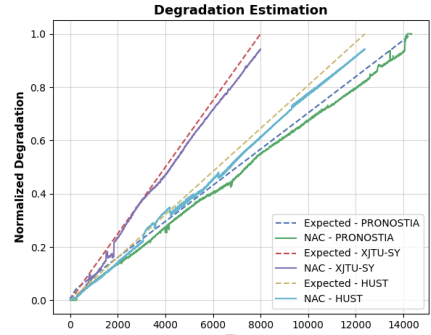


Figure 3. Degradation Estimation Results.

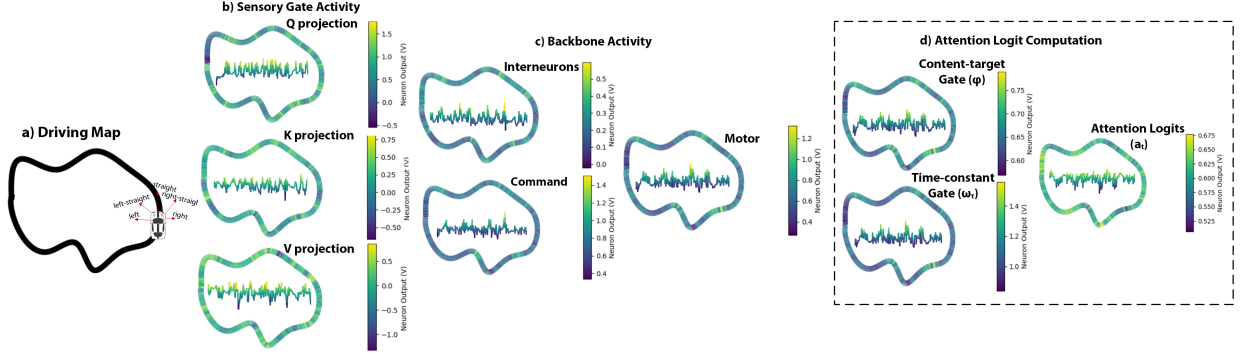


Figure 4. Intuitive visualization of NAC cell activity during driving. (a) NAC-controlled car on the driving map. (b) Sensory gate neurons output (centroid) for the  $q$ ,  $k$ , and  $v$  projections. (c) Backbone neuron activity (centroid), including interneurons, command neurons, and motor neurons. (d)  $\omega_\tau$  and  $\phi$  and  $a_t$  computations. Internal plots show actual neuron activities.

### 3.3. Industry 4.0

Industry 4.0 has revolutionized manufacturing, rendering prognostic health management (PHM) systems indispensable. A key PHM task is estimating the remaining useful life (RUL) of components, particularly rolling element bearings (REB), which account for 40–50% of machine failures (Ding et al., 2021; Zhuang et al., 2021). The objective is to learn degradation features from one operating condition of a dataset and generalize them to unseen conditions within the same dataset. Furthermore, the model should provide accurate RUL estimation on entirely different datasets while maintaining a compact architecture suitable for resource-constrained devices, thereby supporting localized safety.

We utilized three benchmark datasets: (i) PRONOSTIA (Nectoux et al., 2012), (ii) XJTU-SY (Wang et al., 2018), and (iii) HUST (Thuan & Hong, 2023). Training is performed on PRONOSTIA, while XJTU-SY and HUST are used to assess cross-validation. We used the Score metric (Nectoux et al., 2012) to assess the performance. We evaluate generalization using *Bearing 1* from the first operating condition of each dataset. Figure 3 visualizes the expected degradation alongside the outputs of NAC. For the PRONOSTIA dataset, NAC-Exact/05s/8k performed the best, with the lowest score of 37.75. NAC-PW and Contiformer achieved nearly identical scores, with average values of 37.75 and 37.82, respectively. For the XJTU-SY dataset, NAC-Exact/05s/8k has the lowest score of 22.87. CTA ranked second with 25.86, followed by NAC- $\phi$ linear with 29.53. A similar trend was observed on the HUST dataset, where NAC-Exact/05s/8k achieved first place with a score of 27.82, NAC-PW ranked second with 30.14, and NAC- $\phi$ linear ranked third with 35.89. These results demonstrated the strong cross-validation adaptability of NAC.

### 3.4. NAC enhances Interpretability

Interpretability refers to the process of providing explanations that are understandable to humans, either through

visualization or analysis at the neuron cell level. We analyze NAC’s interpretability on OpenAI CarRacing trained with NAC-Steady at two levels: (i) Saliency maps, which use Grad-CAM (Selvaraju et al., 2017) to visualize which features are attended to by the convolutional layers of the model during inference. Additional information on saliency maps is provided in the Appendix D.3.3; (ii) Cell-level neuron state, where we analyze neuron outputs at the cell level, starting from the sensory gates, including the  $q$ ,  $k$ , and  $v$  projections, and extending through the backbone inter-command-motor neurons to the computation of the attention logits. Figure 4 illustrates the cell-level neuron states of NAC. We observe that  $\omega_\tau$  couples its values between 0.8 and 1.6, depending on the input scene. When the car turns left or left-straight, the  $\omega_\tau$  value remains below 1.1. When it turns right or right-straight,  $\omega_\tau$  is maintained above 1.3. In intermediate cases, the model drives straight. This behavior indicates that the evolution of  $\omega_\tau$  changes over time, confirming its input dependency. Similarly, the attention logits reflect this behavior, with a tighter range for left and left-straight actions (below 0.6), higher values for right and right-straight actions (above 0.65), and intermediate values corresponding to straight driving. These cell-level neuron states highlight how activations depend on the input, providing a way to understand and evaluate safety-critical decisions.

### 3.5. Interpreting the Results

We observe that increasing sparsity improves system robustness and leads to higher overall accuracy. Similarly, increasing the number of Top- $K$  interactions improves accuracy, although the benefits diminish. We recommend a Top- $K$  of 8 with 50% sparsity as a robust default for this trade-off. In general, for tasks requiring adaptive CT dynamics due to evolving temporal patterns, use the transient mode (Exact or Euler). For tasks where temporal dynamics are negligible, use the Steady mode.

## 4. Discussions

This paper is part of ongoing research on biologically plausible attention mechanisms and represents a pioneering step, with limitations to be addressed in future work.

**Runtime and Memory Experiment:** The runtime and memory experiments (see Appendix D.4) show that NAC occupies an intermediate position between CT-RNN and CT-Attention baselines in terms of runtime and memory consumption, which could be further improved.

**Architectural improvement:** Currently, NAC uses predetermined wiring (AutoNCP) requiring three inputs: the number of units (sensory + interneuron + motor), motor neurons, and sparsity, with typically 60% of the units assigned to sensory neurons. To integrate with the attention mechanism while preserving wiring, sensory units for  $\mathcal{N}_{\text{sensory}}$  are set as  $\text{units}_{\text{sensory}} = \lceil \frac{d_{\text{model}} - 0.5}{0.6} \rceil$  and backbone units as  $\text{units}_{\text{backbone}} = d_{\text{model}} + \lfloor \frac{d_{\text{model}}}{0.6} \rfloor$ , where  $\lceil \cdot \rceil$  and  $\lfloor \cdot \rfloor$  denote the ceiling and floor functions, respectively. This results in a larger overall architectural size. Future work will support user-defined NCPs configurations or randomized wiring to enable more efficient architectures.

**Learnable sparse Top- $K$  selection:** Sparse Top- $K$  attention can miss important context, is sensitive to  $k$ , and may be harder to optimize. Future work will include learnable Top- $K$  selection, improved key scoring, and hardware-aware optimization to increase accuracy and robustness.

## 5. Conclusion

In this paper, we introduce the Neuronal Attention Circuit (NAC), a biologically inspired attention mechanism that reformulates attention logits as the solution to a first-order ODE modulated by nonlinear, interlinked gates derived from repurposing *C. elegans* nematode NCPs. NAC bridges discrete attention with CT dynamics, enabling adaptive temporal processing without the limitations inherent to traditional scaled dot-product attention. Based on the solution to ODE, we introduce three computational modes: (i) Euler, based on *explicit Euler* integration; (ii) Exact, providing closed-form solutions; and (iii) Steady, approximating equilibrium states. In addition, an adaptable sparse Top- $K$  pairwise concatenation mechanism is implemented to mitigate the quadratic memory footprint. Theoretically, we establish NAC’s logit-state stability and exponential and frozen approximation error bounds, thereby providing rigorous guarantees of convergence and expressiveness. Empirically, we demonstrated that NAC achieves state-of-the-art performance across diverse tasks, including irregularly sampled time-series benchmarks, autonomous vehicle lane-keeping, and industrial prognostics, while being interpretable and explainable. Moreover, NAC occupies an intermediate position between CT-RNNs and CT-Attention in terms of runtime and memory consumption.

## Reproducibility Statement

The code for reproducibility is available at [https://github.com/itxwaleedrazzaq/neuronal\\_attention\\_circuit](https://github.com/itxwaleedrazzaq/neuronal_attention_circuit).

## Impact Statement

This work addresses the growing field of CT-Attention and pioneers a biologically inspired mechanism. It encourages research into sparse, adaptive networks that resemble natural wiring. From a societal perspective, it supports the development of more robust AI in resource-limited settings. Nevertheless, it also raises ethical concerns when applied to areas such as surveillance or autonomous systems.

## References

Introduction to self-driving cars. URL <https://www.udacity.com/course/intro-to-self-driving-cars--nd113>.

Beltagy, I., Peters, M. E., and Cohan, A. Longformer: The long-document transformer. *arXiv preprint arXiv:2004.05150*, 2020.

Bojarski, M., Del Testa, D., Dworakowski, D., Firner, B., Flepp, B., Goyal, P., Jackel, L. D., Monfort, M., Muller, U., Zhang, J., et al. End to end learning for self-driving cars. *arXiv preprint arXiv:1604.07316*, 2016.

Brockman, G., Cheung, V., Pettersson, L., Schneider, J., Schulman, J., Tang, J., and Zaremba, W. Openai gym. *arXiv preprint arXiv:1606.01540*, 2016.

Cao, Y., Li, S., Petzold, L., and Serban, R. Adjoint sensitivity analysis for differential-algebraic equations: The adjoint dae system and its numerical solution. *SIAM journal on scientific computing*, 24(3):1076–1089, 2003.

Chen, R. T., Rubanova, Y., Bettencourt, J., and Duvenaud, D. K. Neural ordinary differential equations. *Advances in neural information processing systems*, 31, 2018.

Chen, Y., Ren, K., Wang, Y., Fang, Y., Sun, W., and Li, D. Conformer: Continuous-time transformer for irregular time series modeling. *Advances in Neural Information Processing Systems*, 36:47143–47175, 2023.

Chien, J.-T. and Chen, Y.-H. Continuous-time attention for sequential learning. In *Proceedings of the AAAI conference on artificial intelligence*, volume 35, pp. 7116–7124, 2021.

Child, R., Gray, S., Radford, A., and Sutskever, I. Generating long sequences with sparse transformers. *arXiv preprint arXiv:1904.10509*, 2019.

Cho, K., Van Merriënboer, B., Gulcehre, C., Bahdanau, D., Bougares, F., Schwenk, H., and Bengio, Y. Learning phrase representations using rnn encoder-decoder for statistical machine translation. *arXiv preprint arXiv:1406.1078*, 2014.

Choromanski, K., Likhoshevstov, V., Dohan, D., Song, X., Gane, A., Sarlos, T., Hawkins, P., Davis, J., Mohiuddin, A., Kaiser, L., et al. Rethinking attention with performers. *arXiv preprint arXiv:2009.14794*, 2020.

d’Ascoli, S., Becker, S., Mathis, A., Schwaller, P., and Kilbertus, N. Odeformer: Symbolic regression of dynamical systems with transformers. *arXiv preprint arXiv:2310.05573*, 2023.

De Brouwer, E., Simm, J., Arany, A., and Moreau, Y. Gru-ode-bayes: Continuous modeling of sporadically-observed time series. *Advances in neural information processing systems*, 32, 2019.

Deng, L. The mnist database of handwritten digit images for machine learning research [best of the web]. *IEEE signal processing magazine*, 29(6):141–142, 2012.

Ding, Y., Jia, M., Miao, Q., and Huang, P. Remaining useful life estimation using deep metric transfer learning for kernel regression. *Reliability Engineering & System Safety*, 212:107583, 2021.

Gu, A., Goel, K., and Ré, C. Efficiently modeling long sequences with structured state spaces. *arXiv preprint arXiv:2111.00396*, 2021.

Hasani, R., Lechner, M., Amini, A., Rus, D., and Grosu, R. Liquid time-constant networks. In *Proceedings of the AAAI Conference on Artificial Intelligence*, volume 35, pp. 7657–7666, 2021.

Hasani, R., Lechner, M., Amini, A., Liebenwein, L., Ray, A., Tschaikowski, M., Teschl, G., and Rus, D. Closed-form continuous-time neural networks. *Nature Machine Intelligence*, 4(11):992–1003, 2022.

Hochreiter, S. The vanishing gradient problem during learning recurrent neural nets and problem solutions. *International Journal of Uncertainty, Fuzziness and Knowledge-Based Systems*, 6(02):107–116, 1998.

Hochreiter, S. and Schmidhuber, J. Long short-term memory. *Neural computation*, 9(8):1735–1780, 1997.

Hong, H. S. and Thuan, N. Hust bearing: a practical dataset for ball bearing fault diagnosis. *Mendeley Data*, 3, 2023.

John, F. On integration of parabolic equations by difference methods: I. linear and quasi-linear equations for the infinite interval. *Communications on Pure and Applied Mathematics*, 5(2):155–211, 1952.

Jordan, M. I. Serial order: A parallel distributed processing approach. In *Advances in psychology*, volume 121, pp. 471–495. Elsevier, 1997.

Lechner, M. and Hasani, R. Mixed-memory rnns for learning long-term dependencies in irregularly sampled time series. 2022.

Lechner, M., Hasani, R. M., and Grosu, R. Neuronal circuit policies. *arXiv preprint arXiv:1803.08554*, 2018.

Lechner, M., Hasani, R., Amini, A., Henzinger, T. A., Rus, D., and Grosu, R. Neural circuit policies enabling auditable autonomy. *Nature Machine Intelligence*, 2(10): 642–652, 2020.

LeCun, Y., Touresky, D., Hinton, G., and Sejnowski, T. A theoretical framework for back-propagation. In *Proceedings of the 1988 connectionist models summer school*, volume 1, pp. 21–28, 1988.

Nectoux, P., Gouriveau, R., Medjaher, K., Ramasso, E., Chebel-Morello, B., Zerhouni, N., and Varnier, C. Pronostia: An experimental platform for bearings accelerated degradation tests. In *IEEE International Conference on Prognostics and Health Management, PHM’12*, pp. 1–8. IEEE Catalog Number: CPF12PHM-CDR, 2012.

Neil, D., Pfeiffer, M., and Liu, S.-C. Phased lstm: Accelerating recurrent network training for long or event-based sequences. *Advances in neural information processing systems*, 29, 2016.

Nishijima, T. Universal approximation theorem for neural networks. *arXiv preprint arXiv:2102.10993*, 2021.

Rangapuram, S. S., Seeger, M. W., Gasthaus, J., Stella, L., Wang, Y., and Januschowski, T. Deep state space models for time series forecasting. *Advances in neural information processing systems*, 31, 2018.

Razzaq, W. and Hongwei, M. Neural circuit policies imposing visual perceptual autonomy. *Neural Processing Letters*, 55(7):9101–9116, 2023.

Razzaq, W. and Zhao, Y.-B. Carle: a hybrid deep-shallow learning framework for robust and explainable rul estimation of rolling element bearings. *Soft Computing*, 29(23): 6269–6292, 2025a.

Razzaq, W. and Zhao, Y.-B. Developing distance-aware uncertainty quantification methods in physics-guided neural networks for reliable bearing health prediction, 2025b. URL <https://arxiv.org/abs/2512.08499>.

Rubanova, Y., Chen, R. T., and Duvenaud, D. K. Latent ordinary differential equations for irregularly-sampled time series. *Advances in neural information processing systems*, 32, 2019.

Rumelhart, D. E., Hinton, G. E., and Williams, R. J. Learning internal representations by error propagation. Technical report, 1985.

Selvaraju, R. R., Cogswell, M., Das, A., Vedantam, R., Parikh, D., and Batra, D. Grad-cam: Visual explanations from deep networks via gradient-based localization. In *Proceedings of the IEEE international conference on computer vision*, pp. 618–626, 2017.

Shibuya, N. Car behavioral cloning, 2017. URL <https://github.com/naokishibuya/car-behavioral-cloning>. Accessed: 2025-10-05.

Shukla, S. N. and Marlin, B. M. Multi-time attention networks for irregularly sampled time series. *arXiv preprint arXiv:2101.10318*, 2021.

Stinchcomb, M. Multilayered feedforward networks are universal approximators. *Neural Networks*, 2:356–359, 1989.

Thuan, N. D. and Hong, H. S. Hust bearing: a practical dataset for ball bearing fault diagnosis. *BMC research notes*, 16(1):138, 2023.

Tiang, Y., Gelernter, J. R., Wang, X., Chen, W., Gao, J., Zhang, Y., and Li, X. Lane marking detection via fast end-to-end deep convolutional neural network that is our patch proposal network (ppn). 2018.

Vaswani, A., Shazeer, N., Parmar, N., Uszkoreit, J., Jones, L., Gomez, A. N., Kaiser, Ł., and Polosukhin, I. Attention is all you need. *Advances in neural information processing systems*, 30, 2017.

Vidulin, V., Lustrek, M., Kaluza, B., Piltaver, R., and Krivec, J. Localization Data for Person Activity. UCI Machine Learning Repository, 2010. DOI: <https://doi.org/10.24432/C57G8X>.

Wang, B., Lei, Y., Li, N., et al. Xjtu-sy bearing datasets. *GitHub, GitHub Repository*, 2018.

Zaheer, M., Guruganesh, G., Dubey, K. A., Ainslie, J., Alberti, C., Ontanon, S., Pham, P., Ravula, A., Wang, Q., Yang, L., et al. Big bird: Transformers for longer sequences. *Advances in neural information processing systems*, 33:17283–17297, 2020.

Zhang, B., Titov, I., and Sennrich, R. Sparse attention with linear units. *arXiv preprint arXiv:2104.07012*, 2021.

Zhuang, J., Dvornek, N., Li, X., Tatikonda, S., Papademetris, X., and Duncan, J. Adaptive checkpoint adjoint method for gradient estimation in neural ode. In *International Conference on Machine Learning*, pp. 11639–11649. PMLR, 2020.

Zhuang, J., Jia, M., Ding, Y., and Ding, P. Temporal convolution-based transferable cross-domain adaptation approach for remaining useful life estimation under variable failure behaviors. *Reliability Engineering & System Safety*, 216:107946, 2021.

## Appendix

### A. Preliminaries

#### A.1. Neuronal Circuit Policies (NCPs)

NCPs represent a biologically inspired framework for developing interpretable neural control agents by adapting the tap-withdrawal circuit found in the nematode *C.elegans* (Lechner et al., 2018). Unlike traditional spiking neural networks, the majority of neurons in this circuit exhibit electronic dynamics, characterized by the passive flow of electrical charges, resulting in graded potentials. NCPs are structured as a four-layer hierarchical architecture comprising sensory neurons ( $N_s$ ), interneurons ( $N_i$ ), command neurons ( $N_c$ ), and motor neurons ( $N_m$ ). The  $N_s$  perceive and respond to external stimulus inputs and are responsible for the initial signal transduction. Each  $N_s$  consists of subneurons  $S_p$  and  $S_n$  and a system variable  $x$ . The activation of  $S_p$  and  $S_n$  depends upon the sign of  $x$ :  $S_p$  becomes activated for  $x > 0$ , whereas  $S_n$  becomes activated for  $x < 0$ . The variable  $x$  is mapped to the membrane potential range of  $[-70 \text{ mV}, -20 \text{ mV}]$ , which is consistent with the biophysical behavior of nerve cells, which typically exhibit a resting potential at  $-70 \text{ mV}$  and an activation potential near  $-20 \text{ mV}$ . Similarly, each  $N_m$  is composed of two subneurons,  $M_p$  and  $M_n$ , and is driven by a controllable variable  $y$ , which also maps to a biologically plausible range  $[-70 \text{ mV}, -20 \text{ mV}]$ . The connections in the NCP architecture are designed to reflect the biological sparsity and abstraction of neural circuits. Specifically, connections from  $N_s$  to  $N_i$  are feedforward, while those between  $N_c$  and  $N_m$  are highly recurrent (Lechner et al., 2018). Figure 1(a) illustrates the connectome of NCPs.

#### A.2. Attention Mechanism

Attention mechanisms have become a cornerstone in modern neural architectures, enabling models to dynamically focus on relevant parts of the input. The concept was first introduced in the context of neural machine translation, where it allows the decoder to weight encoder outputs according to their importance for generating each target token. Given a query vector  $q \in \mathbb{R}^d$ , key vectors  $K = [k_1, k_2, \dots, k_n] \in \mathbb{R}^{n \times d}$ , and value vectors  $V = [v_1, v_2, \dots, v_n] \in \mathbb{R}^{n \times d}$ , the attention mechanism can be expressed in two steps:

1. Compute the scaled dot attention logits:

$$a_i = \frac{q^T k_i}{\sqrt{d}} \quad (21)$$

2. Normalize the logits to obtain attention weights and compute the output:

$$\alpha_i = \text{softmax}(a_i) = \frac{e^{a_i}}{\sum_{j=1}^n e^{a_j}} \quad (22)$$

$$\text{Attention}(q, k, v) = \sum_{i=1}^n \alpha_i v_i \quad (23)$$

Here,  $a_i$  is the raw attention logit between the query and each key, and the scaling factor  $\sqrt{d}$  prevents large dot products from destabilizing the Softmax (Vaswani et al., 2017).

## B. Proofs

In this section, we provide all the proofs.

### B.1. Analyzing Closed-form Solution

#### B.1.1. DERIVING CLOSED-FORM (EXACT) SOLUTION

Although  $\phi$  and  $\omega_\tau$  are nonlinear functions of the input  $\mathbf{u} = [\mathbf{q}; \mathbf{k}]$ , we derive a closed-form solution by treating them as locally constant over the small integration interval for each query–key pair based on frozen-coefficient approximation (John, 1952). Rewrite Eqn. 1 as

$$\frac{da_t}{dt} + \omega_\tau a_t = \phi. \quad (24)$$

The integrating factor is

$$\mu = e^{\left(\int \omega_\tau dt\right)} = e^{\omega_\tau t}. \quad (25)$$

Multiply both sides by  $\mu(t)$ :

$$e^{\omega_\tau t} \frac{da_t}{dt} + \omega_\tau e^{\omega_\tau t} a_t = \phi e^{\omega_\tau t}. \quad (26)$$

Recognizing the left-hand side as the derivative of  $e^{\omega_\tau t} a_t$ :

$$\frac{d}{dt}(e^{\omega_\tau t} a_t) = \phi e^{\omega_\tau t}. \quad (27)$$

Integrate from 0 to  $T$ :

$$e^{\omega_\tau t} a_t - e^0 a_0 = \phi \int_0^T e^{\omega_\tau s} ds. \quad (28)$$

Compute the integral:

$$\int_0^T e^{\omega_\tau s} ds = \frac{1}{\omega_\tau} (e^{\omega_\tau t} - 1). \quad (29)$$

Substitute back:

$$e^{\omega_\tau t} a_t - a_0 = \phi \cdot \frac{e^{\omega_\tau t} - 1}{\omega_\tau}. \quad (30)$$

Rearrange:

$$e^{\omega_\tau t} a_t = a_0 + \frac{\phi}{\omega_\tau} (e^{\omega_\tau t} - 1). \quad (31)$$

Divide both sides by  $e^{\omega_\tau t}$ :

$$a_t = a_0 e^{-\omega_\tau t} + \frac{\phi}{\omega_\tau} (1 - e^{-\omega_\tau t}). \quad (32)$$

Set  $a^* := \frac{\phi}{\omega_\tau}$ . Then  $a_t = a^* + (a_0 - a^*)e^{-\omega_\tau t}$ , is proved.

#### B.1.2. FROZEN COEFFICIENT ERROR ANALYSIS

In this subsection, we analyze the resulting error due to the frozen approximation with respect to the time-varying behavior of  $\phi$  and  $\omega_\tau$ , both mathematically and empirically.

**Theorem 3** (Frozen-Coefficient Approximation Error). *Consider the attention logit ODE*

$$\frac{da(t)}{dt} = -\omega_\tau(t)a(t) + \phi(t), \quad (33)$$

*with time-varying coefficients  $\phi(t)$  and  $\omega_\tau(t) > 0$ . Let  $a_{\text{varying}}(t)$  denote the solution with varying coefficients (numerically integrated) and  $a_{\text{frozen}}(t)$  denote the exact closed-form solution obtained by freezing the coefficients at their initial values  $\phi_0 = \phi(0)$ ,  $\omega_{\tau 0} = \omega_\tau(0)$  over an integration window  $[0, T]$ . Assume that  $\phi(t)$  and  $\omega_\tau(t)$  are Lipschitz continuous in  $t$  with constants  $L_\phi$  and  $L_\omega$  (i.e.,  $|\phi(t) - \phi(s)| \leq L_\phi |t - s|$ ,  $|\omega_\tau(t) - \omega_\tau(s)| \leq L_\omega |t - s|$ ). Define  $C = |a_0| + |\phi_0|/\omega_{\tau 0}$ . Then, for any  $t \in [0, T]$ , the error  $\varepsilon(t) = a_{\text{varying}}(t) - a_{\text{frozen}}(t)$  satisfies*

$$|\varepsilon(t)| \leq (L_\phi + CL_\omega) t^2 e^{L_\omega t}, \quad (34)$$

*For small  $L_\omega t \ll 1$ , this simplifies to  $\mathcal{O}(t^2)$ .*

*Proof.* The frozen-coefficient solution satisfies

$$\frac{da_{\text{frozen}}}{dt} = -\omega_{\tau 0} a_{\text{frozen}} + \phi_0, \quad a_{\text{frozen}}(0) = a(0), \quad (35)$$

Subtracting Eqn. 35 from Eqn. 33 yields the error dynamics

$$\frac{d\varepsilon}{dt} = -\omega_{\tau 0} \varepsilon + \delta\phi(t) + \delta\omega_\tau(t) a_{\text{varying}}(t), \quad (36)$$

where  $\delta\phi(t) = \phi(t) - \phi_0$  and  $\delta\omega_\tau(t) = \omega_{\tau 0} - \omega_\tau(t)$ . By Lipschitz,  $|\delta\phi(t)| \leq L_\phi t$  and  $|\delta\omega_\tau(t)| \leq L_\omega t$ . Using the integrating factor  $e^{\omega_{\tau 0} t}$ ,

$$\frac{d}{dt}(e^{\omega_{\tau 0} t} \varepsilon(t)) = e^{\omega_{\tau 0} t} (\delta\phi(t) + \delta\omega_\tau(t) a_{\text{varying}}(t)), \quad (37)$$

Integrating from 0 to  $T$  and noting that  $\varepsilon(0) = 0$ ,

$$\varepsilon(t) = \int_0^T e^{-\omega_{\tau 0}(t-s)} (\delta\phi(s) + \delta\omega_{\tau}(s)a_{\text{varying}}(s)) ds, \quad (38)$$

The frozen solution from Eqn. 32 is

$$a_{\text{frozen}}(s) = a_0 e^{-\omega_{\tau 0}s} + \frac{\phi_0}{\omega_{\tau 0}} (1 - e^{-\omega_{\tau 0}s}), \quad (39)$$

so that  $|a_{\text{frozen}}(s)| \leq C$ . Hence  $|a_{\text{varying}}(s)| \leq C + |\varepsilon(s)|$ . Taking absolute values in Eqn. 38 and using Lipschitz bounds,

$$|\varepsilon(t)| \leq \int_0^T e^{-\omega_{\tau 0}(t-s)} (L_{\phi}s + L_{\omega}s(C + |\varepsilon(s)|)) ds, \quad (40)$$

Since  $e^{-\omega_{\tau 0}(t-s)} \leq 1$ ,

$$|\varepsilon(t)| \leq (L_{\phi} + CL_{\omega})t^2 + L_{\omega} \int_0^T |\varepsilon(s)| ds. \quad (41)$$

Applying Gronwall's inequality to  $|\varepsilon(t)|$  yields

$$|\varepsilon(t)| \leq (L_{\phi} + CL_{\omega})t^2 e^{L_{\omega}t}, \quad (42)$$

which is Eqn. 34. Expanding the exponential for  $L_{\omega}t \ll 1$  gives the  $\mathcal{O}(t^2)$  bound.  $\square$

**Empirical Analysis:** We now empirically analyze the error introduced by freezing  $\phi(t)$  and  $\omega_{\tau}(t)$ . We evaluate the closed-form frozen solution against continuously varying coefficients. Empirical analysis across four regimes: (i) slow variation (gradual linear change); (ii) fast variation (exponential growth); (iii) step changes (abrupt discontinuities); and (iv) oscillatory behavior (periodic modulation) shows that the frozen approximation maintains bounded error even under substantial parameter variation. Table 2 summarizes the empirical results. For typical slow-varying irregular sequences, with  $\phi$  varying by 0.5% and  $\omega_{\tau}$  varying by 0.26%, the frozen solution exhibits minimal error, with a mean of 1.87%, and a maximum of 3.05%. Even under more challenging regimes, the error remains predictable and bounded, reaching 6.41% for fast variation, 6.53% for step changes, and 7.81% for oscillatory behavior. An illustration of oscillatory evolution is shown in Figure 5.

*Interpretation:* Given that the variation rates in real-world irregular sequences rarely exceed 10%, these results confirm the adequacy of the frozen approximation for practical deployment. We therefore recommend *Exact* as the default computation mode for NAC while preserving adaptive Euler integration for edge cases with exceptionally rapid dynamics.

## B.2. Proof of Theorem 1

We divide the proof into two parts: (i) the single-connection case  $M = 1$ , and (ii) the general multi-connection case

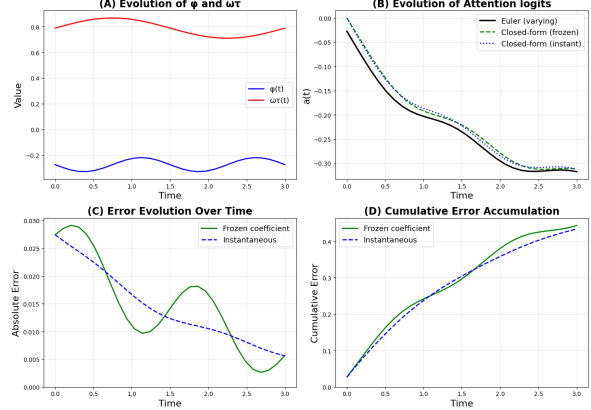


Figure 5. Visualization of oscillatory evolution of NAC.

Table 2. Empirical error analysis of frozen-coefficient approximation across variation regimes.

| Variation   | mean (%)    | max (%)     | $\phi$ (%)  | $\omega_{\tau}$ (%) |
|-------------|-------------|-------------|-------------|---------------------|
| Slow        | 1.87        | 3.05        | 0.50        | 0.26                |
| Fast        | 6.41        | 6.50        | 2.63        | 1.58                |
| Step        | 6.53        | 7.20        | 3.51        | 2.11                |
| Oscillatory | 7.81        | 6.90        | 8.28        | 2.10                |
| Average     | <b>5.65</b> | <b>5.18</b> | <b>3.73</b> | <b>1.51</b>         |

$M > 1$ . The main technique is to evaluate the ODE at boundary values of the proposed invariant interval and show that the derivative points inward, ensuring that trajectories cannot escape.

CASE 1: SINGLE CONNECTION ( $M = 1$ ).

The ODE reduces to

$$\frac{da}{dt} = -\omega_{\tau}a + \phi = -\omega_{\tau}(a - A), \quad A = \frac{\phi}{\omega_{\tau}}. \quad (43)$$

Here  $A$  is the unique equilibrium. We now check both bounds.

- *Upper bound:* Let  $M = \max(0, A)$ . At  $a = M$ ,

$$\frac{da}{dt} \Big|_{a=M} = -\omega_{\tau}(M - A). \quad (44)$$

If  $A \geq 0$ , then  $M = A$  and  $\frac{da}{dt} = 0$ . If  $A < 0$ , then  $M = 0$ , so  $\frac{da}{dt} = -\omega_{\tau}(0 - A) = \omega_{\tau}A \leq 0$  since  $A < 0$ . In both cases,  $\frac{da}{dt} \leq 0$ . Thus trajectories cannot cross above  $M$ .

- *Lower bound:* Let  $m = \min(0, A)$ . At  $a = m$ ,

$$\frac{da}{dt} \Big|_{a=m} = -\omega_{\tau}(m - A). \quad (45)$$

If  $A \leq 0$ , then  $m = A$  and  $\frac{da}{dt} = 0$ . If  $A > 0$ , then  $m = 0$ , so  $\frac{da}{dt} = -\omega_{\tau}(0 - A) = \omega_{\tau}A \geq 0$ . In both cases,

$\frac{da}{dt} \geq 0$ . Thus trajectories cannot cross below  $m$ . Therefore, the interval  $[m, M]$  is forward-invariant.

To see this explicitly under Euler discretization with step size  $\Delta t > 0$ ,

$$a(t + \Delta t) = a_t + \Delta t \cdot \frac{da}{dt}. \quad (46)$$

At  $a = M$ ,  $\frac{da}{dt} \leq 0 \implies a(t + \Delta t) \leq M$ . At  $a = m$ ,  $\frac{da}{dt} \geq 0 \implies a(t + \Delta t) \geq m$ . By induction over steps,  $a_t \in [m, M]$  for all  $t \in [0, T]$ .

CASE 2: MULTIPLE CONNECTIONS ( $M > 1$ ).

The ODE is

$$\frac{da}{dt} = -\left(\sum_{j=1}^M f_j\right)a + \sum_{j=1}^M f_j A_j, \quad (47)$$

with per-connection equilibria  $A_j = \phi_j/f_j$ . The effective equilibrium is

$$A = \frac{\sum_{j=1}^M f_j A_j}{\sum_{j=1}^M f_j}. \quad (48)$$

Since the weights  $\frac{f_j}{\sum f_j}$  are positive and sum to 1,  $A$  is a convex combination of  $\{A_j\}$ . Therefore,

$$A \in [A^{\min}, A^{\max}]. \quad (49)$$

- *Upper bound:* Let  $M = \max(0, A^{\max})$ . Then

$$\frac{da}{dt} \Big|_{a=M} = \sum_{j=1}^M f_j (A_j - M). \quad (50)$$

Since  $A_j \leq A^{\max} \leq M$ , each term  $(A_j - M) \leq 0$ , and thus  $\sum f_j (A_j - M) \leq 0$ . Hence  $\frac{da}{dt} \leq 0$ , proving trajectories cannot exceed  $M$ .

- *Lower bound:* Let  $m = \min(0, A^{\min})$ . Then

$$\frac{da}{dt} \Big|_{a=m} = \sum_{j=1}^M f_j (A_j - m). \quad (51)$$

Since  $A_j \geq A^{\min} \geq m$ , each  $(A_j - m) \geq 0$ , so  $\sum f_j (A_j - m) \geq 0$ . Hence  $\frac{da}{dt} \geq 0$ , proving trajectories cannot fall below  $m$ . Thus, the interval  $[m, M]$  is forward-invariant.

*Remark 1.* This result guarantees that the continuous-time attention state converges within a well-defined interval dictated by the per-connection equilibria. In particular, for the single-connection case ( $M = 1$ ), the state trajectory converges monotonically toward the closed-form equilibrium solution (Eqn. 18) without overshoot.

### B.3. Proof for Theorem 2

The proof proceeds constructively by showing that the NAC layer can emulate a single-hidden-layer feedforward neural network with nonlinear activations, which is a universal approximator under the Universal Approximation Theorem (UAT). We assume self-attention on a single-token input  $x \in \mathbb{R}^n$  (setting sequence length  $T = 1$ ) and focus on the steady mode for simplicity. Without loss of generality, set  $d_{\text{model}} = n + m$  or adjust as needed for dimensionality. Constructively, set NCP sparsity  $s = 0$  for full connectivity, ensuring the backbone  $\mathcal{NN}_{\text{backbone}}$  approximates any  $\tilde{\phi} : \mathbb{R}^{2d} \rightarrow [0, 1]$  with error  $< \delta$  via stacked layers. For multi-head, scale  $H$  proportionally to target complexity, with output projection  $W_o$  aggregating as in classical UAT proofs (Stinchcomb, 1989).

**Input Projections:** The input  $x$  is projected via NCP-based sensory projections to obtain query  $q = q_{\text{proj}}(x)$ , key  $k = k_{\text{proj}}(x)$ , and value  $v = v_{\text{proj}}(x)$ , each in  $\mathbb{R}^{d_{\text{model}}}$ . For emulation, set  $q_{\text{proj}} = k_{\text{proj}} = I_n$  (identity on  $\mathbb{R}^n$ ) and adjust  $W_v$  later, so  $q = k = x$  and  $v$  is configurable. These are affine transformations and do not limit expressivity.

**Head Splitting and Sparse Top- $k$  Pairwise Computation:** Split into  $H$  heads, yielding  $q^{(h)}, k^{(h)} \in \mathbb{R}^d$  per head  $h$ , where  $d = d_{\text{model}}/H$ . For  $T = 1$ , compute sparse top- $k$  pairs, but since  $T = 1$ ,  $K_{\text{eff}} = 1$ , yielding concatenated pair  $u^{(h)} = [q^{(h)}; k^{(h)}] \in \mathbb{R}^{2d}$ . Since  $q^{(h)} = k^{(h)}$ , this is  $[x^{(h)}; x^{(h)}]$ , but the NCP processes it generally.

**Computation of  $\phi^{(h)}$  and  $\omega_{\tau}^{(h)}$ :** The scalar  $\phi^{(h)}$  is computed via the NCP-based inter-to-motor projection on the pair:

$$\phi^{(h)} = \sigma(\mathcal{NN}_{\text{backbone}}(u^{(h)})) \quad (52)$$

where  $\sigma(z) = (1 + e^{-z})^{-1}$  is the sigmoid. This NCP, with sufficiently large units and low sparsity, approximates any continuous scalar function  $\tilde{\phi} : \mathbb{R}^{2d} \rightarrow [0, 1]$  to arbitrary precision on compact sets (by the UAT for multi-layer networks (Stinchcomb, 1989)). Similarly,  $\omega_{\tau}^{(h)}$  is computed via:

$$\omega_{\tau}^{(h)} = \text{softplus}(\mathcal{NN}_{\text{backbone}}(u^{(h)})) + \varepsilon, \quad \varepsilon > 0 \quad (53)$$

By setting weights to make  $\omega_{\tau}^{(h)} \equiv 1$  (constant), the steady-mode logit simplifies to  $a^{(h)} = \phi^{(h)}/\omega_{\tau}^{(h)} = \phi^{(h)}$ . Thus,  $a^{(h)} \approx \sigma(w^{(h)}x + b^{(h)})$  for chosen weights  $w^{(h)}, b^{(h)}$ , emulating a sigmoid hidden unit.

**Attention Weights and output:** For  $T = 1$ , the softmax over one “key” yields  $\alpha^{(h)} = \exp(a^{(h)})/\exp(a^{(h)}) = 1$ . The head output is  $y^{(h)} = \int_T \alpha^{(h)} v^{(h)} dt$ . Set  $v_{\text{proj}}$  such that  $v^{(h)} = 1$  (scalar), yielding  $y^{(h)} \approx \sigma(w^{(h)}x + b^{(h)})$ . For vector-valued  $v^{(h)}$ , more complex combinations are possible, but scalars suffice here.

**Output Projection:** Concatenate head outputs:  $Y = [y^{(1)}; y^{(2)}; \dots; y^{(H)}] \in \mathbb{R}^H$ . Apply the final dense layer:

$$g(x) = (Y \cdot W_o) + b_o \in \mathbb{R}^m. \quad (54)$$

With  $y^{(h)} \approx \sigma(w^{(h)}x + b^{(h)})$ , this matches a single-hidden-layer network with  $H$  units. By the UAT, for large  $H$ , such networks approximate any continuous  $f$  on compact  $K$  to accuracy  $\epsilon$ , by choosing appropriate  $w^{(h)}, b^{(h)}, W_o, b_o$ .

## C. Training, Gradients and Complexity

### C.1. Gradient Characterization

We analyze the sensitivity of the dynamics with respect to the underlying learnable parameters. Specifically, we compute closed-form derivatives of both the steady state and the full trajectory  $a_t$  with respect to the parameters  $\phi$  and  $\omega_\tau$ . These expressions illuminate how gradients flow through the system, and provide guidance for selecting parameterizations that avoid vanishing or exploding gradients.

#### C.1.1. TRAJECTORY SENSITIVITIES FOR CLOSED-FORM FORMULATION

The trajectory is given by

$$a_t = a^* + (a_0 - a^*)e^{-\omega_\tau t}, \quad (55)$$

which depends on  $(\phi, \omega_\tau)$  both through the equilibrium  $a^*$  and the exponential term.

**Derivative with respect to  $\phi$ :** We obtain

$$\frac{\partial a_t}{\partial \phi} = \frac{1 - e^{-\omega_\tau t}}{\omega_\tau} \quad (56)$$

*Interpretation:* For large  $\omega_\tau$ , the gradient with respect to  $\phi$  saturates quickly but shrinks to scale  $\mathcal{O}(1/\omega_\tau)$ , potentially slowing learning of  $\phi$ . Conversely, very small  $\omega_\tau$  leads to large steady-state gradients, which may destabilize optimization.

**Derivative with respect to  $\omega_\tau$ :** Here, both the equilibrium and the decay rate depend on  $\omega_\tau$ , yielding

$$\frac{\partial a_t}{\partial \omega_\tau} = -\frac{\phi}{\omega_\tau^2} (1 - e^{-\omega_\tau t}) - (a_0 - a^*) t e^{-\omega_\tau t}. \quad (57)$$

*Interpretation:* The gradient with respect to  $\omega_\tau$  contains a transient term proportional to  $te^{-\omega_\tau t}$ , which dominates at intermediate times, and a steady-state contribution proportional to  $-\phi/\omega_\tau^2$ , which persists asymptotically. Thus, sensitivity to  $\omega_\tau$  is time-dependent, peaking before vanishing exponentially in the transient component.

### C.2. Efficiency and Complexity

Table 3 summarizes the computational complexity of different sequence models. For sequence prediction over length  $n$  with hidden dimension  $k$ , RNNs scale linearly,  $\mathcal{O}(nk)$ , while Attention scale quadratically,  $\mathcal{O}(n^2k)$ . ODE-based models, such as LNNs, incur an additional multiplicative factor  $S$  for the number of solver steps. NAC scale  $\mathcal{O}(n\sqrt{nk})$ .

For single-time-step prediction, RNNs, LSTMs, and NAC require  $\mathcal{O}(k)$ , whereas Attention and NAC require  $\mathcal{O}(nk)$  when recomputing attention over the full sequence.

### C.3. Gradient-Based Training

Like Neural ODEs (Chen et al., 2018) and CT-RNNs (Rubanova et al., 2019), NAC produces differentiable computational graphs and can be trained using gradient-based optimization, such as the adjoint sensitivity method (Cao et al., 2003) or backpropagation through time (BPTT) (Le-Cun et al., 1988). In this work, we use BPTT exclusively, as the adjoint sensitivity method can introduce numerical errors (Zhuang et al., 2020).

Table 3. Sequence and time-step prediction complexity.  $n$  is the sequence and  $k$  is the hidden/model dimension.

| Model          | Sequence                  | Time-step                |
|----------------|---------------------------|--------------------------|
| RNN            | $\mathcal{O}(nk)$         | $\mathcal{O}(k)$         |
| Attention      | $\mathcal{O}(n^2k)$       | $\mathcal{O}(nk)$        |
| LNN (ODEsolve) | $\mathcal{O}(nk \cdot S)$ | $\mathcal{O}(k \cdot S)$ |
| NAC-Exact      | $\mathcal{O}(n\sqrt{nk})$ | $\mathcal{O}(nk)$        |

## D. Evaluation

### D.1. Related Works

The brief descriptions of related works are divided into four subcategories.

**DT-RNNs:** RNN (Rumelhart et al., 1985) captures sequential dependencies in time-series data by updating a hidden state from the current observation and the previous state. LSTM (Hochreiter & Schmidhuber, 1997) extends RNNs with input, output, and forget gates, allowing the network to maintain and update long-term memory, which improves the modeling of long-term dependencies in time-series sequences. GRU (Cho et al., 2014) simplifies the LSTM architecture by combining the forget and input gates into a single update gate, allowing efficient modeling of long-term dependencies in time-series sequences.

**CT-RNNs:** CT-RNN (Rubanova et al., 2019) models temporal dynamics using differential equations, enabling hidden states to evolve continuously over time in response to inputs, which is particularly useful for irregularly sampled time-series data. PhasedLSTM (Neil et al., 2016) introduces a time gate that updates hidden states according to a rhythmic schedule, enabling efficient modeling of asynchronous or irregularly sampled time-series. GRU-ODE (De Brouwer et al., 2019) extends the GRU to continuous time, evolving hidden states via ODEs to handle sequences with nonuniform time intervals. mmRNN (Lechner & Hasani, 2022) combines short-term and long-term memory units to capture both fast-changing and slowly evolving patterns in sequential data. LTC (Hasani et al., 2021) uses neurons

with learnable, input-dependent time constants to adapt the speed of dynamics and capture complex temporal patterns in continuous-time data. CfC (Hasani et al., 2022) approximate LTC dynamics analytically, providing efficient continuous-time modeling without relying on numerical ODE solvers. DeepState (Rangapuram et al., 2018) combines RNNs with linear state-space models (SSMs), allowing the RNN to produce time-varying SSM parameters to model CT dynamics. S4 (Gu et al., 2021) parametrizes SSMs with a structured low-rank correction to the state matrix, enabling efficient convolution-based computation and effective modeling of long-range dependencies.

**DT-Attentions:** Attention (Vaswani et al., 2017) computes attention weights by measuring the similarity between queries and keys, scaling the results, and applying Softmax to weigh time-step contributions. Multihead attention (Vaswani et al., 2017) applies multiple parallel scaled dot-product attention mechanisms, capturing different types of temporal dependencies simultaneously for complex time-series modeling. Linear Attention (Zhang et al., 2021) replaces the softmax activation with a *ReLU* function to induce sparsity and enable heads to selectively switch off for certain queries. Performer (Choromanski et al., 2020) approximates Softmax attention with linear-time FAVOR+, enabling efficient and scalable Attention without losing theoretical guarantees.

**CT-Attentions:** mTAN (Shukla & Marlin, 2021) learns continuous-time embeddings and uses time-based attention to interpolate irregular observations into a fixed-length representation for downstream encoder-decoder modeling. CTA (Chien & Chen, 2021) generalizes discrete-time attention to continuous-time by representing hidden states, context vectors, and attention scores as functions whose dynamics are modeled via neural networks and integrated using ODE solvers for irregular sequences. ODEFormer(d’Ascoli et al., 2023) trains a sequence-to-sequence transformer on synthetic trajectories to directly output a symbolic ODE system from noisy, irregular time-series data. ContiFormer (Chen et al., 2023) builds a CT-Transformer by pairing ODE-defined latent trajectories with a time-aware attention mechanism to model dynamic relationships in irregular time-series data.

## D.2. Ablations Details

The brief descriptions of variants and ablation are divided into five subcategories:

**Top- $K$  Ablations:** *NAC-2k* uses Top- $K=2$  to compute the logits and *NAC-32k* uses Top- $K=32$ . *NAC-PW* uses fully pairwise (no sparsity) concatenation. All variants use the exact computation mode with 50% sparsity.

**NAC-Sparsity Ablations:** *NAC-02s* uses 20% sparsity to compute the logits, and *NAC-09s* uses 90%. All variants use the exact computation mode with Top- $K=8$  and  $\delta_t=1.0$ .

**NAC with isolated NCPs Ablations:** To isolate the effect of the NCP gating mechanism, we ablate it using MLP layers with matched sparsity. *NAC-FC* replaces the gating module with a standard fully connected layer. *NAC-09sFC* applies 90% sparsity, *NAC-05s* applies 50% sparsity, and *NAC-02s* applies 20% sparsity. All variants use the exact computation mode with Top- $K = 8$  and  $\delta_t=1.0$ .

**NAC with unconstrained  $\phi$ :** Applying a sigmoidal nonlinearity to  $\phi$  yields the logit to only positive values. To allow negative logits, we tested two variants: (i) *NAC- $\phi_{linear}$*  with no activation, and (ii) *NAC- $\phi_{tanh}$*  with a tanh activation.

**Modes Ablations:** *NAC-Euler* computes attention logits using the explicit Euler integration method. *NAC-Steady* derives attention logits from the steady-state solution of the exact formulation. *NAC-Exact/05s/8k* computes attention logits using the closed-form exact solution. It also overlaps with other ablations, so we combined it into a single one. All modes use Top- $K=8$ , 50% sparsity and  $\delta_t=1.0$ .

## D.3. Experimental Details

### D.3.1. EVENT-BASED MNIST

**Dataset Explanation and Curation:** The MNIST dataset, introduced by (Deng, 2012), is a widely used benchmark for computer vision and image classification tasks. It consists of 70,000 grayscale images of handwritten digits (0–9), each of size  $28 \times 28$  pixels, split into 60,000 training and 10,000 testing samples.

**Preprocessing:** We follow the preprocessing pipeline described in (Lechner & Hasani, 2022), which proceeds as follows. First, a threshold is applied to convert the 8-bit pixel values into binary values, with 128 as the threshold on a scale from 0 (minimum intensity) to 255 (maximum intensity). Second, each  $28 \times 28$  image is reshaped into a one-dimensional time-series of length 784. Third, the binary time-series is encoded in an event-based format, eliminating consecutive occurrences of the same value; for example, the sequence [1, 1, 1, 1] is transformed into (1,  $t = 4$ ). This encoding introduces a temporal dimension and compresses the sequences from 784 to an average of 53 time steps. Finally, to facilitate efficient batching and training, each sequence is padded to a fixed length of 256, and the time dimension is normalized such that each symbol corresponds to one unit of time. The resulting dataset defines a per-sequence classification problem on irregularly sampled time-series.

**Neural Network Architecture:** We develop an end-to-end hybrid neural network by combining compact convolutional layers with NAC or counterparts baselines for fair comparison. Detailed hyperparameters and architectural specifications are provided in Table 4.

### D.3.2. PERSON ACTIVITY RECOGNITION (PAR)

**Dataset Explanation and Curation:** We used the Localized Person Activity Recognition dataset provided by UC Irvine (Vidulin et al., 2010). The dataset comprises 25 recordings of human participants performing different physical activities. The eleven possible activities are “walking,” “falling,” “lying down,” “lying,” “sitting down,” “sitting,” “standing up from lying,” “on all fours,” “sitting on the ground,” “standing up from sitting,” and “standing up from sitting on the ground.” The objective of this experiment is to recognize the participant’s activity from inertial sensors, formulating the task as a per-time-step classification problem. The input data consist of sensor readings from four inertial measurement units placed on participants’ arms and feet. While the sensors are sampled at a fixed interval of 211 ms, recordings exhibit different phase shifts and are thus treated as irregularly sampled time-series.

**Preprocessing:** We first separated each participant’s recordings based on sequence identity and calculated elapsed time in seconds using the sampling period. To mitigate class imbalance, we removed excess samples from overrepresented classes to match the size of the smallest class. Subsequently, the data were normalized using a standard scaler. Finally, the dataset was split into 9:1 ratio for training and testing.

**Neural Network Architecture:** Following the approach in Section D.3.1, we developed an end-to-end neural network combining convolutional heads with NAC or other baselines. Hyperparameter details are summarized in Table 4.

### D.3.3. AUTONOMOUS VEHICLE

**Dataset Explanation and Curation:** We followed the data collection methodology described in (Razzaq & Hongwei, 2023). For OpenAI-CarRacing, a PPO-trained agent (5M timesteps) was used to record 20 episodes, yielding approximately 48174 RGB images of size  $92 \times 92 \times 3$  with corresponding action labels across five discrete actions (no-act, move left, forward, move right, stop). The dataset was split with 10% reserved for testing and the remaining 90% for training. For the Udacity simulator, we manually controlled the vehicle for 50 minutes, producing 15647 RGB images of size  $320 \times 160 \times 3$ , captured from three camera streams (left, center, right) along with their corresponding continuous steering values. This dataset was split into 20% testing and 80% training.

**Preprocessing:** No preprocessing was applied to the OpenAI-CarRacing dataset. For the Udacity simulator, we followed the preprocessing steps in (Shibuya, 2017). Each image was first cropped to remove irrelevant regions and resized to  $66 \times 120 \times 3$ . Images were then converted from RGB to YUV color space to match the network input. To improve robustness, data augmentation techniques, including random flips, translations, shadow overlays, and brightness variations, were applied to simulate lateral shifts and diverse

lighting conditions.

**Neural Network Architecture:** For OpenAI-CarRacing, we modified the neural network architecture proposed in (Razzaq & Hongwei, 2023), which combines compact CNN layers for spatial feature extraction with LNNs to capture temporal dynamics. In our implementation, the LNN layers were replaced with NAC and its comparable alternatives for fair evaluation. Full hyperparameter configurations are provided in Table 4. For the Udacity simulator, we modified the network proposed in (Bojarski et al., 2016) by replacing three latent MLP layers with NAC and its counterparts. Full hyperparameters are summarized in Table 4.

**Saliency Maps:** A saliency map visualizes the regions of the input that a model attends to when making decisions. Figure 6 shows the saliency maps for the OpenAI CarRacing environment. We observe that only NAC (Steady, Euler, and Steady) maintains focus on the road’s horizon, while other models either focus on the sides or remain largely unresponsive to the task. Figure 7 also presents the saliency maps for the Udacity Simulator. In this case, NAC-Exact, CTA produce the most accurate visual maps, maintaining attention on the road’s horizon, followed by ContiFormer and mTAN, which achieve comparable performance. MHA, Linear Attention, Performer, and PhasedLSTM also generate reasonable saliency maps, although their focus is more dispersed across the scene. In contrast, other models either fail to identify relevant regions, producing blurry maps, or focus solely on one side of the road. These results demonstrate that NAC exhibits interpretable attention patterns in the underlying task.

### D.3.4. INDUSTRY 4.0

**Dataset Explanation and Curation:** *PRONOSTIA dataset* is a widely recognized benchmark dataset in the field of condition monitoring and degradation estimation of rolling-element bearings. Nectoux et al. (Nectoux et al., 2012) developed this dataset as part of the PRONOSTIA experimental platform. The dataset comprises 16 complete run-to-failure experiments performed under accelerated wear conditions across three different operating settings: 1800 rpm with 4 kN radial load, 1650 rpm with a 4.2 kN load, and 1500 rpm with a 5 kN load, all at a frequency of 100 Hz. Vibration data were recorded using accelerometers placed along the horizontal and vertical axes, which were sampled at 25.6 kHz. Additionally, temperature readings were collected at a sampling rate of 10 Hz.

*XJTU-SY Dataset* is another widely recognized benchmark dataset developed through collaboration between Xi’an Jiaotong University and Changxing Sumyoung Technology (Wang et al., 2018). The dataset comprises 15 complete run-to-failure experiments performed under accelerated degradation conditions with three distinct operational settings: 1200 rpm (35 Hz) with a 12 kN radial load, 2250 rpm (37.5 Hz)

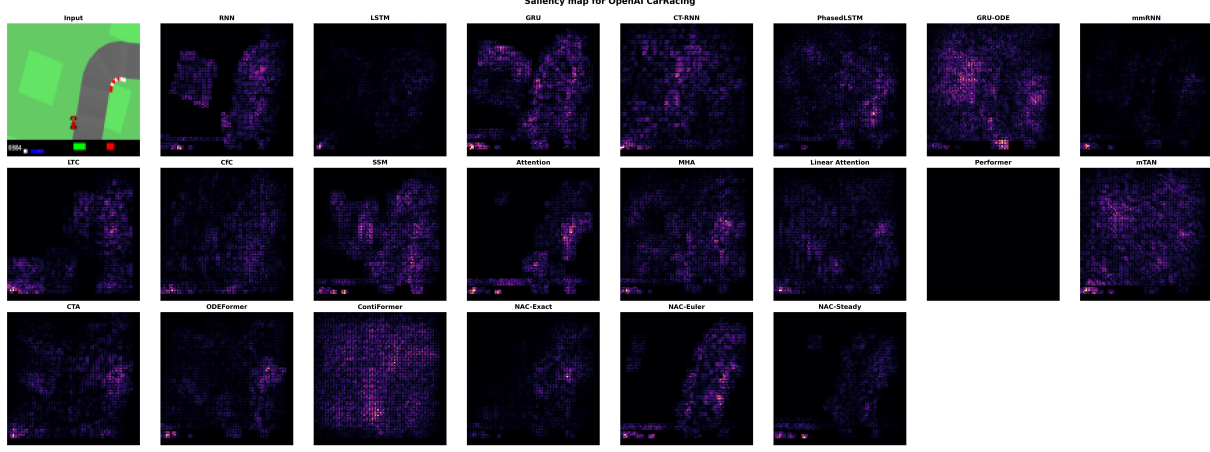


Figure 6. Saliency maps for OpenAI CarRacing

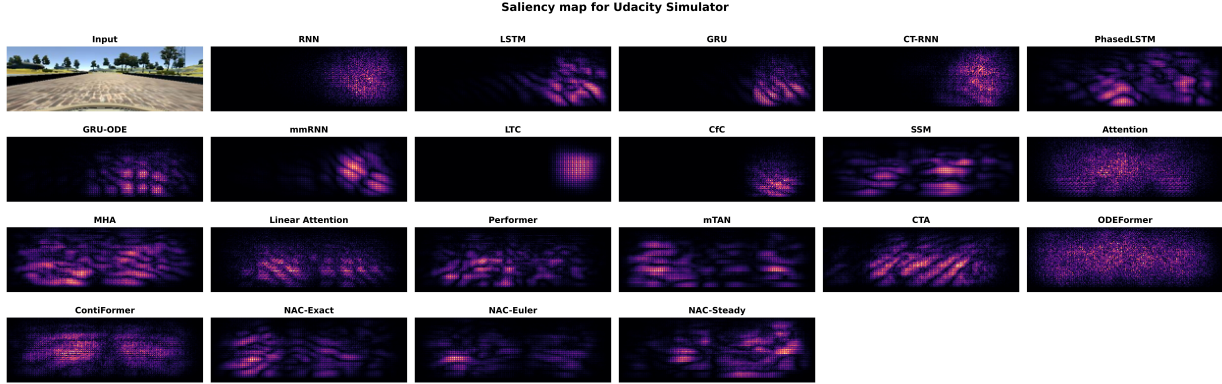


Figure 7. Saliency maps for Udacity Simulator

Table 4. Summary of Key Hyperparameters of All Experiments

| Param.      | MNIST      | PAR            | CarRacing          | Udacity              | RUL EST.         |
|-------------|------------|----------------|--------------------|----------------------|------------------|
| Conv layers | 2x1D(64@5) | 1D(64@5, 64@3) | 3xTD-2D(10-30@3-5) | 5x2D(24-64@5-3, ELU) | 2x1D(32@3, 16@2) |
| NAC         | 64-d, 8h   | 32-d, 4h       | 64-d, 16h          | 100-d, 20h           | 16-d, 8h         |
| Dense       | 32-10(SM)  | 32-11(SM)      | 64-5(SM)           | 64-1(Lin)            | 1(Lin)           |
| Dropout     | —          | —              | 0.2                | 0.5                  | —                |
| Opt.        | AdamW      | AdamW          | Adam               | AdamW                | AdamW            |
| LR          | 0.001      | 0.001          | 0.0001             | 0.001                | 0.001            |
| Loss        | SCE        | SCE            | SCE                | MSE                  | MSE              |
| Metric      | Acc        | Acc            | Acc                | MAE                  | Score            |
| Batch       | 32         | 20             | 32                 | —                    | 32               |
| Epochs      | 150        | 500            | 100                | 10                   | 150              |

**Note:** SCE = Sparse Categorical Crossentropy; Acc = Accuracy; MAE = Mean Absolute Error; MSE = Mean Squared Error; SM = softmax; Lin = Linear; TD = TimeDistributed; Conv1D/2D = Conv1D/2D;  $d$  = model dimension;  $h$  = attention heads.

**Baselines Hyperparameters Clarification:** All (CT & DT) RNNs use the same number of hidden units as NAC's  $d_{model}$ , and all (DT & CT) Attention use the same  $d_{model}$  and *heads* as NAC. The other layers, including 1D/2D, Dense, and the remaining hyperparameters, are the same during our tests.

with an 11 kN radial load, and 2400 rpm (40 Hz) with a 10 kN radial load. Vibrational signals were recorded using an accelerometer mounted on the horizontal and vertical axes and sampled at 25.6 kHz. This dataset is only used for the

cross-validation test.

**HUST Dataset** is a practical dataset developed by Hanoi University of Science and Technology to support research on ball bearing fault diagnosis (Hong & Thuan, 2023). The

dataset includes vibration data collected from five bearing types (6204, 6205, 6206, 6207, and 6208) under three different load conditions: 0 W, 200 W, and 400 W. Six fault categories were introduced, consisting of single faults (inner race, outer race, and ball) and compound faults (inner–outer, inner–ball, and outer–ball). Faults were created as early-stage defects in the form of 0.2 mm micro-cracks, simulating real degradation scenarios. The vibration signals were sampled at 51.2 kHz with approximately 10-second recordings for each case. This dataset is only used for the cross-validation test.

**Preprocessing:** Condition monitoring data comprises 1D non-stationary vibrational signals collected from multiple sensors. To extract meaningful information, these signals must be transformed into features that possess meaningful physical interpretability. We utilized the preprocessing proposed in (Razzaq & Zhao, 2025a), and physically plausible labels are generated according to (Razzaq & Zhao, 2025b). Initially, the signal is segmented into small, rectangularized vectors using a windowing technique, enabling better localization of transient characteristics. The continuous wavelet transform (CWT) with the Morlet wavelet as the mother wavelet is then applied to obtain a time-frequency representation (TFR). The CWT is defined as  $\Gamma(a, b) = \int_{-\infty}^{\infty} x_w(t) \frac{1}{\sqrt{a}} \psi^* \left( \frac{t-b}{a} \right) dt$ , where  $a$  and  $b$  denote the scale and translation parameters, respectively, and  $\psi$  is the Morlet wavelet function. From the TFR, a compact set of statistical and domain-specific features is extracted to characterize the operational condition of the bearing.

**Neural Network Architecture:** The objective of this problem is to design a compact neural network that can effectively model degradation dynamics while remaining feasible for deployment on resource-constrained devices, enabling localized and personalized prognostics for individual machines. To achieve this, we combine a compact convolutional network with NAC. The CNN component extracts spatial degradation features from the training data, while NAC performs temporal filtering to emphasize informative features. This architecture maintains a small model size without sacrificing representational capacity. Full hyperparameter configurations are reported in Table 4.

**Evaluation Metric:** Score is a metric specifically designed for RUL estimation in the IEEE PHM (Nectoux et al., 2012) to score the estimates. The scoring function is asymmetric, penalizing overestimations more heavily than early predictions. This reflects practical considerations, as late maintenance prediction can lead to unexpected failures with more severe consequences than early intervention can.

$$Score = \sum_{i: \hat{y}_i < y_i} \left( e^{-\frac{\hat{y}_i - y_i}{13}} - 1 \right) + \sum_{i: \hat{y}_i \geq y_i} \left( e^{\frac{\hat{y}_i - y_i}{10}} - 1 \right) \quad (58)$$

Table 5. Run-Time and Memory Benchmark Results

| Model              | Run-Time (s)         | Throughput (seq/s) | Peak Memory (MB) |
|--------------------|----------------------|--------------------|------------------|
| RNN                | 1.8392 $\pm$ 0.1933  | 0.544              | 0.29             |
| CT-RNN             | 7.1097 $\pm$ 0.3048  | 0.141              | 0.67             |
| LSTM               | 2.6241 $\pm$ 0.2906  | 0.381              | 0.42             |
| PhasedLSTM         | 4.9812 $\pm$ 0.272   | 0.201              | 0.80             |
| GRU                | 3.216 $\pm$ 0.2566   | 0.311              | 0.54             |
| GRU-ODE            | 12.2498 $\pm$ 0.0525 | 0.082              | 0.64             |
| mmRNN              | 7.5852 $\pm$ 0.2785  | 0.132              | 0.96             |
| LTC                | 14.643 $\pm$ 0.2445  | 0.068              | 0.99             |
| CfC                | 6.0988 $\pm$ 0.2135  | 0.164              | 0.76             |
| DeepState          | 0.6246 $\pm$ 0.0301  | 1.60               | 2.10             |
| S4                 | 0.0182 $\pm$ 0.0003  | 54.95              | 66.98            |
| Attention          | 0.0016 $\pm$ 0.0001  | 625.00             | 16.86            |
| MHA                | 0.0041 $\pm$ 0.0001  | 243.90             | 69.05            |
| Linear Attention   | 0.0088 $\pm$ 0.0015  | 113.81             | 43.7             |
| Performer          | 0.0097 $\pm$ 0.0019  | 102.94             | 18.57            |
| mTAN               | 0.0272 $\pm$ 0.0054  | 36.76              | 790.16           |
| ODEFormer          | 0.0317 $\pm$ 0.0016  | 31.55              | 67.71            |
| CTA                | 8.5275 $\pm$ 0.2355  | 0.117              | 1.43             |
| ContiFormer        | 0.066 $\pm$ 0.0075   | 15.15              | 67.71            |
| NAC-2k             | 7.3071 $\pm$ 0.1547  | 0.137              | 44.75            |
| NAC-32k            | 7.2313 $\pm$ 0.2119  | 0.138              | 549.86           |
| NAC-PW             | 8.5649 $\pm$ 0.0203  | 0.117              | 5042.09          |
| NAC-09s            | 7.222 $\pm$ 0.176    | 0.139              | 150.85           |
| NAC-02s            | 7.252 $\pm$ 0.2018   | 0.138              | 151.54           |
| NAC- $\phi$ linear | 7.223 $\pm$ 0.164    | 0.138              | 150.85           |
| NAC- $\phi$ tanh   | 7.232 $\pm$ 0.1045   | 0.138              | 151.54           |
| NAC-FC             | 0.0588 $\pm$ 0.0043  | 20.48              | 24.57            |
| NAC-09sFC          | 0.0521 $\pm$ 0.0048  | 19.38              | 24.34            |
| NAC-05sFC          | 0.0516 $\pm$ 0.0049  | 19.18              | 24.09            |
| NAC-02sFC          | 0.0495 $\pm$ 0.0056  | 18.73              | 24.34            |
| NAC-Exact/05s/8k   | 7.4101 $\pm$ 0.1586  | 0.135              | 151.50           |
| NAC-Euler          | 7.3367 $\pm$ 0.1719  | 0.136              | 152.22           |
| NAC-Steady         | 7.2942 $\pm$ 0.1451  | 0.137              | 150.86           |

#### D.4. Run Time and Memory Experiments

We evaluate the computational requirements on fixed-length sequences of 1024 steps, 64-dimensional features, 4 heads, and a batch size of 1. Each model is run for ten forward passes on Google Colab T4-GPU, and we report the mean runtime with standard deviation, throughput, and peak memory usage. NAC occupies an intermediate position in runtime relative to several CT-RNN models, including GRU-ODE, CfC, and LTC. In terms of memory consumption, NAC uses significantly less memory than mTAN does, with NAC-2k being the least memory-consuming among the CT-Attention models. Reducing the NAC sparsity from 90% to 20% has a minimal effect on memory, decreasing usage slightly from 151.54 MB to 150.85 MB. In contrast, decreasing the Top- $K$  selection from PW to  $k = 2$  drastically reduces the memory consumption from 5042 MB to 44.75 MB, demonstrating the flexibility of NAC.